Phylogeny

270 Million Years

Dragonfly

Damselfly

Predation

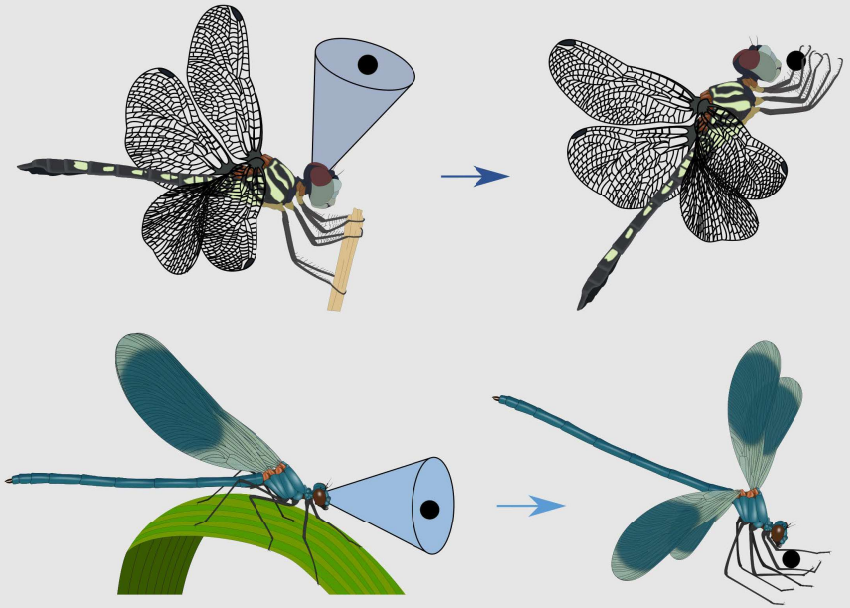

Homologous pre-motor target tracking neurons

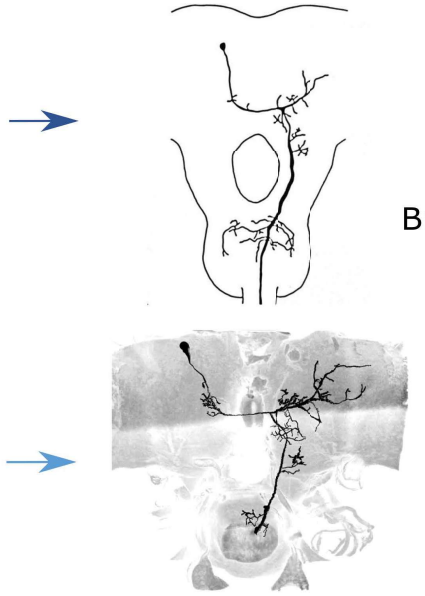

Encoding of target movement by Target Selective Descending Neurons

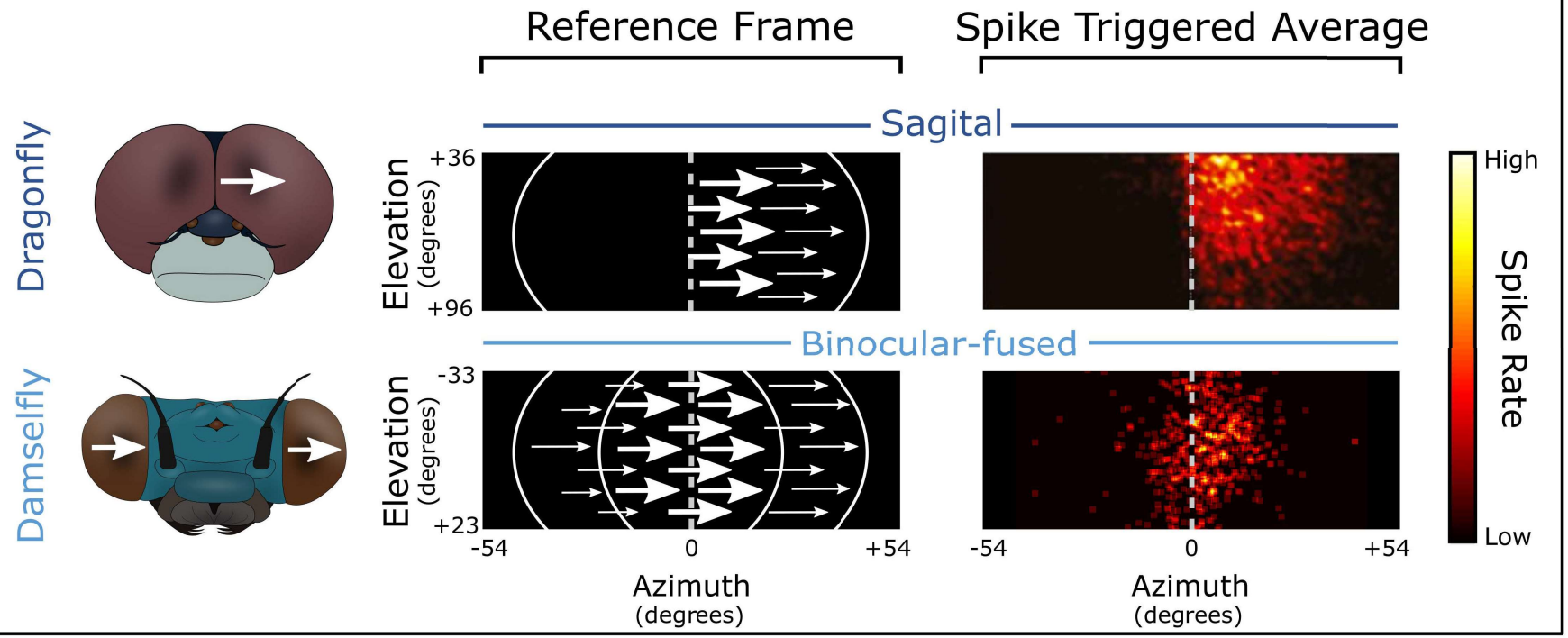

Binocular encoding in the damselfly premotor target tracking system

Authors: Jack A. Supple[1], Daniel Pinto-Benito[1], Christopher Khoo[1], Trevor J. Wardill[2], Samuel T. Fabian[1], Molly Liu[2], Siddhant Pusdekar[2], Daniel Galeano[2], Jintao Pan[3], Shengdian Jiang[3], Yimin Wang[3,4], Lijuan Liu[3], Hanchuan Peng[3], Robert M. Olberg[5], Paloma T. Gonzalez-Bellido[2*]

[1] Department of Physiology, Development, and Neuroscience, University of Cambridge, Downing Street, Cambridge CB3 2EG, UK.

[2] Department of Ecology, Evolution, and Behavior, University of Minnesota, Saint Paul, MN 55108, USA.

[3] SEU-Allen Joint Center, Institute for Brain and Intelligence, Southeast University, Nanjing, 210096, China.

[4] School of Computer Engineering and Science, Shanghai University, Shanghai, 200444, China.

[5] Department of Biological Sciences, Union College, New York, 12308, USA.

* Corresponding Author: paloma@umn.edu

Lead contact: paloma@umn.edu

Summary

Akin to all damselflies, *Calopteryx* (family *Calopterygidae*), commonly known as jewel wings or demoiselles, possess dichoptic (separated) eyes with overlapping visual fields of view. In contrast, many dragonfly species possess holoptic (dorsally fused) eyes with limited binocular overlap. We have here compared the neuronal correlates of target tracking between damselfly and dragonfly sister lineages and linked these changes in visual overlap to premotor neural adaptations. While dragonflies attack prey dorsally, we show that demoiselles attack prey frontally. We identify demoiselle Target Selective Descending Neurons (TSDNs) with matching frontal visual receptive fields, anatomically and functionally homologous to the dorsally-positioned dragonfly TSDNs. By manipulating visual input using eyepatches and prisms, we show that moving target information at the premotor level depends on binocular summation in demoiselles. Consequently, demoiselles encode directional information in a binocularly fused frame of reference such that information of a target moving towards the midline in the left eye is fused with information of the target moving away from the midline in the right eye. This contrasts with dragonfly TSDNs where receptive fields possess a sharp midline boundary, confining responses to a single visual hemifield in a sagittal frame of reference (i.e. relative to the midline). Our results indicate that although TSDNs are conserved across Odonata, their neural inputs, and thus the upstream organization of the target tracking system, differs significantly and match divergence in eye design and predatory strategies.

Introduction

Despite sampling the visual world through two eyes, our brain fuses these images into a cyclopean percept with a single point of view [1]. Binocular image fusion imparts several perceptual advantages including enhanced visual sensitivity [2,3], decreased reaction times [4], and the potential to calculate depth from image disparity [5,6]. As such, binocularity is often found in visually guided predatory species [7].

Odonata is an ancient predatory lineage comprising two distinctive extant sister groups, the damselflies (Zygoptera) and dragonflies (Epiprocta, comprising Anisoptera and Epiophlebioptera) (Figure S1A). Damselflies and dragonflies share a last common ancestor ~270 Million Years Ago (MYA) and have subsequently diverged in behaviour and anatomy [8,9]. Dragonflies are well known for their large round compound eyes and agile interception flights to catch flying prey [10]. To date, a large body of work describes the behavioural and neurophysiological mechanisms underlying target interception in dragonflies [10–18]. Such studies have focused on abundant Anisopteran dragonflies (families *Aeshnoidea*, *Corduliidae*, and *Libellulidea*) that intercept prey from below, stabilising the prey image upon a cyclopean dorsal fovea [10–18]. This fovea is formed by fusing the compound eyes at the dorsal surface into a continuous plane of ommatidia with reduced binocular overlap, known as a holoptic eye [19].

Target movement across the dragonfly dorsal fovea (Figure 1Ai) is encoded at the pre-motor level by a small population of eight bilaterally symmetric Target Selective Descending Neurons (TSDNs) [11,13,20]. TSDNs receive input from the lateral protocerebrum, and project to the suboesophageal ganglion (SOG) and thoracic motor centres with a total latency of less than 30 ms [11,13,20]. Each TSDN type possesses a characteristic receptive field that is directionally tuned and spatially localised to a specific region of the dorsal visual field [11]. As a population, TSDNs primarily encode target movement away from or along the midline [11] and TSDN firing can change the angle of attack and beating of the wings [21,22], presumably reflecting their role as part of a reactive steering mechanism keeping the dragonfly locked onto the prey during pursuit [11].

The holoptic eye morphology of extant dragonflies appears to be a secondarily derived trait, which has evolved repeatedly within the Odonatoptera superorder throughout the last 320 MYA [8,23]. Holoptic eyes are absent in all damselflies, several extant dragonfly lineages (families *Gomphoidea*, *Petaluroidea*, and the basal dragonfly lineage *Epiophlebiidae)* (Figure S1A) and extinct archaic Odonatopterans [24]. Instead, all damselflies have two conspicuously separated (dichoptic) compound eyes [9,25]. Hitherto, little is known about the anatomical and neuronal specializations facilitating predation in any damselfly [25]. While most damselflies are known to hunt by snatching stationary prey from a substrate, a behaviour termed gleaning [9,26], the demoiselle damselflies (*Calopterygidae*) are thought only to attack flying prey [9,27], somewhat similar to dragonflies. Demoiselles are thus uniquely placed within Zygoptera to investigate how frontal facing foveae with large interocular distance (Figure 1Aii) may influence prey tracking circuits, especially in comparison to those described in dragonflies.

In this study we investigate how the divergences between damselflies and dragonflies at the level of visual anatomy are reflected in their predatory tactic and target tracking circuitry. In comparison to dragonflies, we found that damselflies attack when their prey is positioned more frontally, rather than dorsally, in the visual field. We also report that this frontal area of the visual field in damselflies is sampled by TSDNs homologous to those of dragonflies. Unlike the holoptic dragonflies studied to date, all TSDNs responses in damselflies integrate information from both eyes and they encode target direction in a binocular, fused reference frame. This is distinctly different from holoptic dragonflies, whose TSDNs encode direction of a moving target in a sagittal reference frame relative to the midline formed by their two merged eyes.

Results

Demoiselles attack prey head on

As previously reported [10,12,15], we found that dragonflies approach their prey from below (Figure 1Bi, Video S1), tracking targets within the dorsal fovea. Just prior to, and throughout the flight, the prey

aligned above the dragonfly body azimuth on average 32.6° (95% confidence interval (CI) = ± 12.4°, n=8) and 33.7° (95% CI = ± 5.3°, n=8), respectively (Figures 1C, Figure S1B, Video S1).

In contrast, we found that damselflies fly to the elevation of the target (Figure 1Bii), keeping it in the frontal aspect of their visual field before lunging forwards to grasp it (Video S2). We found that just prior to, and throughout the flight, the prey aligned above the demoiselle body azimuth on average 13.9° (95% CI = ± 13.0°, n=5) and 11.4° (95% CI = ± 6.5°, n=10), respectively (Figure 1C, Figure S1B, Video S2).

Both measures of prey location here reported, i.e., above the body axis prior to the initiation of flight, and throughout flight, were statistically significantly different between dragonflies and demoiselles ($p = 0.0441$, and $p = 6.98e\text{-}05$, respectively, Watson-Williams tests).

TSDNs serving the demoiselle frontal fovea

We next investigated how the more frontal predatory behaviour and dichoptic ocular arrangement of demoiselles is reflected in their target-tracking system. In multiunit recordings from the demoiselle ventral nerve cord, responses to small moving objects were confined to the frontal visual field (Figure 2A). Thus, we positioned the animals and visual stimuli accordingly (Figure 2B, Figure S2A-B). We first recorded target responses from the ventral nerve cord with extracellular tungsten electrodes, and after spike sorting (Figure S2C, STAR methods), we calculated the latency (Figure S3A-B), spike triggered averages, and directional tuning maps (Figure S3C).

We discovered demoiselle descending neurons that shared distinguishing features with dragonfly TSDNs: (i) robust responses to small targets of fixed size that moved in cardinal directions, (ii) directional tuning, and (iii) no sustained responses to wide-field stimuli (Figure S3C) [11,13]. We classified these cells as demoiselle TSDNs and assigned them to previously described dragonfly TSDN cell types [11] according to the position and direction tuning of their receptive fields (Figure 2C and Figure S3, we putatively recorded the following number of cells for each TSDN type MDT1 =12, MDT2 = 6, MDT3 = 4, MDT4 = 8 , MDT5 = 4, DIT1 =5 , DIT2 = 9, DIT3 = 7). We found that the response properties of demoiselle TSDNs are qualitatively very similar in directional selectivity to those

123 previously described in dragonflies [11], and the overall tuning curves for moving targets appears to be
124 remarkably conserved (Figure 2C, Figure S3C).

125 We hypothesized that demoiselle TSDNs would not only be functionally similar to dragonfly TSDNs,
126 but also anatomically similar. To link anatomy and function, we recorded the responses from the
127 demoiselle TSDNs intracellularly (Figure 2C, rows marked '*') and loaded them with fluorescent dye
128 at the end of the recording. The receptive field location and the directional tuning of these intracellularly
129 identified neurons were consistent with those isolated extracellularly (Figure 2C), validating our
130 extracellularly recorded receptive fields. Our intracellular maps appear sparser due to a reduced
131 mapping stimulus (1.3 vs 20 minutes), as we aimed to maximize time for dye loading. Lines of activity
132 are observed due to the longer, rasterised target trajectories presented across the visual field with this
133 reduced stimulus. The cell body position and arborisation pattern of all demoiselle TSDNs (Video S3
134 and S4) matched closely those of dragonflies (Figure 3) [13,20], with the majority of demoiselle TSDN
135 cell bodies (i.e. DIT1, DIT2, MDT2, MDT4, MDT5) also arising from the n-ventral cell body cluster
136 ('n-' relative to the neuraxis [28]). Together, the anatomical and electrophysiological properties of
137 demoiselle TSDNs demonstrates that these neurons are homologous.

138 Our intracellular recordings highlight the variability in the number of spikes (Figure 4), and the
139 extensive bilateral location of the receptive fields. Given these properties, responses to moving targets
140 alone are not sufficient to distinguish with absolute certainty between some TSDNs, even though we
141 always recorded from the right connective in demoiselles. This is the case for all three ipsilateral cells
142 responsive to targets moving towards the right of the animal (MDT2/DIT2/MDT3). The same ambiguity
143 exists between the two contralateral cells responsive to targets moving towards the left (DIT1/DIT3).
144 This ambiguity, however, does not change the conclusions from our findings, in this or the following
145 sections. Our intracellular dataset also highlights that both the spike rate and overall binocular extent
146 of a single TSDN type can differ substantially across animals (Figure 4). In addition to the high
147 variability of responses within TSDN types, our recordings points towards the possibility that more than
148 eight pairs of forward looking TSDNs exist in demoiselles (see Figure S4).

Whilst demoiselle and dragonfly TSDNs share many characteristics, we also found important differences, most strikingly in the extent of overlap across the visual midline (Figure 2C). The receptive fields of most dragonfly TSDNs display a sharp vertical boundary at or just over the midline, confining responses to target movement within a single hemifield [11]. Only two dragonfly TSDNs (DIT3 and MDT3), exhibit responses that extend more than 10° into the opposing hemifield, and the responses within only that opposing hemifield are not directionally tuned (Figure 2C) [11]. In contrast, the receptive fields of demoiselle TSDNs often extend beyond 20° across the visual midline and maintain the directional tuning across both hemifields (Figure 2C, 4, and S3C). Next, we investigated how such bilateral receptive fields arise in demoiselle damselflies.

Demoiselle damselfly TSDNs are binocular, and exhibit binocular-only, ocular-balanced, or ocular-dominant responses

To investigate how the extension of receptive fields across the visual midline in demoiselle TSDNs relates to inputs from either eye, we recorded TSDN responses under monocular conditions where one eye was occluded with an opaque eye patch. Compared to the uncovered control conditions, all TSDNs exhibited a significant drop in spike numbers when either eye was covered (Friedman test for repeated measures with *post hoc* sign test, $p = 0.00014$, $n = 12$; Figure 5, Figure S5B), demonstrating that demoiselle TSDNs depend upon simultaneous binocular inputs. For all cells recorded, the hemifield ipsilateral to the patched eye had very low activity relative to controls (Figure 5A-C, relative response integral <0.5; Figure S5B), which is consistent with the patch fully occluding visual input from that side. However, we saw varying responses in the hemifield that corresponded to the unoccluded eye, which we will refer to the "contralateral hemifield" (as it is contralateral to the patch). We categorised these responses into three types.

In Type 1 responses, the contralateral hemifield activity was low regardless of whether the patch was on the right or left (Figure S5A), indicating these responses belonged to neurons that were exclusively binocular with visual responses dependent on both eyes contributing in an all (binocular) or none (monocular) fashion (Figure 5A, $n = 3$ cells from 2 animals, Figure S5B). Very few spikes were observed in each monocular condition, and those present were mostly in the non-occluded visual

hemifield, suggesting that the contralateral eye was not accidentally occluded (Figure 5A). This binocular-only group implies that for these neurons, monocular responses to a moving target do not reach the threshold required to fire the TSDN, but that such threshold is reached by the combination of both monocular responses at or upstream of the TSDN (Figure 5A model).

Type 2 responses exhibited moderate, if variable, activity in the contralateral hemifield whether the patch was on the left or right eye. (Figure S5, n = 4 cells from 4 animals). Hence, in TSDNs with Type 2 responses (Figure 5B), the single unoccluded eye that was not patched sufficiently excited the neuron to fire. We speculate that the input weighting from each eye is balanced in these neurons, and by combining the two monocular responses, binocular contributions synergise to increase spike numbers across the entire receptive field (Figure 5B model). It is possible that the difference between Type 1 and Type 2 responses are due to different spiking thresholds (i.e. sensitivity) at the time of the experiment (Figure 5B, model), a TSDN property that we had previously observed in our intracellular recordings (Figure 4).

Type 3 responses were asymmetrical in that we observed contralateral hemifield activity when the patch was on the right, but not when the patch was on the left (Figure S5, n = 5 cells from 5 animals). Hence, the neurons in this category exhibit 'left ocular dominance'. This response pattern could arise from a similar summation-to-threshold mechanism as Type 2 responses, but with ocular weightings that are not balanced, and thus only one visual hemifield can reach threshold under monocular conditions (Figure 5C, model). It is possible that the different threshold sensitivities and ocular weightings are in fact invariant properties of individual TSDNs types, but we cannot resolve if this is the case from our extracellular data in this experiment, because some of the TSDN responses have directional tuning responses and receptive field locations similar to each other (but see Figure S5B for putative TSDN ID allocation for the recordings in this experiment).

Differences in global light level do not underlie the binocular input requirements of TSDNs

Our results above demonstrate that target tracking at the pre-motor stage in demoiselles depends on binocular input. Do TSDNs require that both eyes perceive a discrete moving target, or is the observed

dependence a result of a decrease in global luminance in the patched eye (see for example [29])? To test this possibility, we compared monocular responses resulting from eyepatches made of either an opaque or translucent material (Figure 6A, n = 3 cells from 2 animals. Cells 1 and 2 were recorded simultaneously from the same animal). Note that for this experiment a reduced mapping stimulus was used (also chosen for intracellular recordings). This resulted in sparser receptive field maps, with lines of activity arising from the longer, rasterised target trajectories presented across the visual field. This stimulus choice aimed to maximise the number of conditions per recording. The translucent eyepatch functioned to diffuse target contrast details within the visual field, such that no TSDN target responses were observed when both eyes were covered, although overall changes in light level still made the neuron fire, as seen in the preservation of wide-field ON-OFF responses (Figure S6A-B). All three types of binocular responses described above were observed again under both opaque and translucent monocular conditions, with no obvious differences in spike firing rates between the two eyepatch materials (Figure 6A). This demonstrates that the abolition of demoiselle TSDN spike firing for Type 1 responses and the reduction of spike firing in the contralateral uncovered visual hemifield of Type 2 and 3 responses does not arise from global luminance intensity differences between both eyes. Instead, this lack of response appears to result from an unsatisfied requirement of demoiselle TSDNs for simultaneous stimulation of each eye by a moving target.

Demoiselle TSDN receptive fields resulting from reduced binocularity are consistent with binocular summation

Given that target-tracking responses from both eyes are necessary to drive demoiselle TSDNs effectively, we next investigated whether reducing the level of binocular overlap between the two eyes would result in similarly dramatic changes to the TSDNs receptive fields. We speculated that a small decrease in binocular overlap (i.e. 4^{o}) would not have a significant impact in the ability of the TSDN to summate to threshold over the majority of its response, and thus spike numbers would be similar to control. In contrast, a large drop in binocular overlap (i.e. 10^{o}), should result in the TSDN failing to reach threshold, and thus lead to a lower number of spikes.

For this test, we placed wedge prisms in front of one or both eyes that deviated the visual scene by either 4º or 10º to the left of the animal. When placed over only the left eye, the prism decreases binocular overlap compared to uncovered controls (Figure S6C). As a control, we placed prisms over both eyes, shifting the entire visual field to the left. As expected, shifting global visual input also shifted the receptive field with the 4º prism (two-sided sign test for matched pairs, 4° deviation: $p = 0.004$, Figure 6B, blue densities). The receptive field also shifted under 10º prism although it did not reach statistical significance (two-sided sign test for matched pairs, 10° deviation: $p = 0.07$; Figure 6B, blue densities). The receptive field densities continue to resemble Gaussian distributions when the prism covers both eyes. Subtracting the prism-both shifted density from that of the uncovered condition generates a curve anti-symmetric about the vertical axis, resembling a sinusoid, as expected for two Gaussians of similar width and offset medians (Figure 6B, bottom row, B-U).

When we used a prism over the left eye to reduce binocular overlap by 4°, there was no significant reduction in spike density within the receptive field (two-sided sign test for matched pairs, $p = 1.0$, $n = 9$ cells from 6 animals, Figure 6B). This is in contrast to the attenuation observed in monocular occluding experiments (Figure 5 and 6A), and is consistent with summation of two monocular responses, with the offset monocular response (left eye) still sufficiently overlapping with the other (right eye) to reach threshold when combined. Indeed, under these 4° deviation conditions, the receptive field widens to the left (Figure 6B, ellipses) with a higher number of spikes seen in the entirety of the left hemifield (Figure 6B, bottom row, compare L-U and B-U, thin lines). This is as expected from monocular inputs that are moved further apart, albeit still overlapping in their areas of peak sensitivity. In contrast, when a more powerful prism reduced binocular overlap by 10°, the relative response within the receptive field was attenuated significantly (two-sided sign test for matched pairs, $p = 0.0078$, $n = 8$ cells from 7 animals; Figure 4B, compare purple densities and bottom row L-U). This indicates that at this deviation power, the two monocular responses are sufficiently offset such that the summed TSDN response is no longer able to reach threshold, analogous to what was observed under monocular occluding conditions (Figure 5 and 6A).

Discussion

Hunting strategy, eye morphology, and TSDN homology within Odonata

Damselflies and dragonflies share a last common ancestor ~270 MYA and have thereafter evolved distinct behavioural and anatomical divergence, most notably in predatory tactic [9], flight kinematics [30], and ocular configuration [8,9,25]. Dichoptic eyes resembling those of Zygoptera and lower Epiprocta are present in fossils of extinct early Odonates [8,24] suggesting a dichoptic ancestral morphology among Odonata. Our behavioural data demonstrates, with regards to body orientation, the more frontal angle of attack in demoiselles compared to the dorsal path of Libellulid dragonflies (Figure 1 B-C and S1B-C).

Although our high-speed videos do not have the resolution required to quantify the orientation of the head axis relative to the body axis, we know that an offset between these two axes exists in the dragonfly and demoiselle species here investigated. For example, when *Erythemis simplicicollis* is perched in our arena in preparation for hunting, we estimate that the head is tilted ventrally by ~30° with regards to the body axis (Figure S1D). Similarly, when ready for hunting, a demoiselle perches with its body axis pitched downward (~12°), and with its head pitched dorsally by the same amount (Figure S1E). Therefore, we estimate that on average, *E. simplicicollis* responds to prey that is ~63° above the dragonfly head axis (Figure S1D). This is consistent with the high acuity dorsal fovea of this species, which is positioned at 60° elevation [10], and within the preferred hunting range of 57° to 102° in elevation previously reported for common white tail dragonflies (*P. lydia*) [15]. Likewise, we can estimate that, on average, a demoiselle responds when the prey is flying ~2° above its head axis (Figure S1E). This also fits well with the location of the visual fovea published for other damselfly species as directed forward and slightly downward [25,31]. Given such estimations, we predict that the differences in the attack (i.e. dorsal-dragonfly and frontal-demoiselle) here reported between the two groups would be even more pronounced if the measurements of the prey elevation were made relative to the head axis instead (i.e. prey location within the visual field of the predator).

Together, the behaviour and the alignment of homologous TSDN receptive fields to the frontal and dorsal aspect of the visual field respectively (Figures 2, 3 and S2), suggests that an ancestral target

281 tracking neuronal circuitry was inherited by these sister lineages and co-evolved with divergent ocular
282 anatomy and predatory strategies.

283 Despite the distal ancestry between damselflies and dragonflies, TSDN receptive field architecture and
284 anatomy are remarkably conserved (Figures 2, 3). Demoiselle TSDNs are directionally tuned, with
285 some demoiselle TSDNs often indistinguishable from those in the dragonfly based on directional
286 selectivity. This was somewhat surprising given the dissimilarity in flight kinematics in these sister
287 lineages [30], and suggests that pre-motor encoding is robust to peripheral idiosyncrasies in flight
288 actuation. It would be interesting to compare motor circuitry downstream of TSDNs in the thoracic
289 motor centres to investigate whether peripheral circuitry is similarly robust to flight kinematics or
290 whether these circuits are the subject of specialisation [32].

291 ## Neuronal encoding of holoptic versus dichoptic visual space

292 Holoptic eyes have evolved independently in other insect lineages, and aside from dragonflies are
293 especially common amongst dipteran males who intercept or pursue fast flying females, including
294 hoverflies, horseflies, and soldierflies [19]. Functionally, holoptic eyes are believed to aid in tracking
295 small fast moving targets, although this is mechanistically poorly understood [19]. For example,
296 holoptic eyes are usually associated with a dorsal bright or acute zone where resolution is increased by
297 flattening the ommatidial plane to reduce interommatidial angles [19,33], however, this advantage alone
298 is attainable without dorsal fusion of the eyes, as is found in robberflies [34] and mantids [35].

299 Our comparative work suggests that in Odonata the reference frame within which a target is encoded
300 differs between holoptic and dichoptic eyes. Because demoiselle TSDNs are directionally tuned, and
301 because their responses are dependent on the summation of input from both eyes, they encode
302 directional information in a binocular-fused frame of reference i.e. information of a target moving
303 towards the midline in the left eye must be combined with information of the target moving away from
304 the midline in the right eye. This is in contrast to the TSDNs of holoptic *Aeshnoidea* and *Libellulidea*
305 dragonflies, whose receptive fields possess a sharp midline boundary [11,13,20], and thus encode target
306 motion with a frame of reference that is relative to their sagittal plane. It is possible that the sharpening

of this midline boundary in dragonfly TSDNs has co-evolved with the holoptic eye, and functions to simplify the pre-motor representation of the visual scene by encoding movement of targets in each eye as two halves of a visual panorama. This sagittal reference frame explicitly represents target movement with respect to the holoptic midline, and thus aligns the sensory coordinate system to represent lateralised commands for the thoracic motor centres. This design may enhance the efficiency of neuronal processing for rapid and accurate responses in interception strategies that do not require stereoscopic information, as is thought to be the case in *Libellulidea* [15]. We would expect other holoptic species to employ a similarly lateralised simplification of premotor target movement representations.

Binocular properties of demoiselle TSDNS

We have shown that the responses of demoiselle TSDNs to small moving targets are highly or entirely dependent on simultaneous binocular stimulation (Figures 5-6). In insects, binocular neurons that assess self-motion through wide-field optic flow includes those of the lobula complex [36–38], descending neurons [39,40], and motor neurons [41]. Such binocular wide field neurons respond strongly to monocular stimulation, and binocular integration functions to extend the receptive field across the visual panorama to enhance directional selectivity and match specific modes of self-motion [36,38,40,41]. Further studies document binocular integration of moving objects in the lobula complex of crabs, mantids, and dragonflies [17,42,43]. The dragonfly centrifugal neuron (CSTMD1) responds to small moving objects with an extended receptive field across the two visual hemispheres, and is thought to attend to targets moving from one visual hemisphere to the other [17]; in this respect the function of binocular integration appears to be to extend the receptive field, similar to binocular optic flow neurons [36]. In crabs and mantids, lobula neurons typically respond to independent monocular stimulation with vertical bars, but simultaneous stimulation of both eyes changes (increases or decreases) those responses [42,43]. In the case of mantids, binocular responses are consistent with a linear summation to threshold mechanism [43]. Thus, given that demoiselle TSDNs appear to sum monocular responses to threshold (Figure 5), it is possible that mantis and demoiselle object tracking circuits may integrate binocular information similarly, earlier in the visual system.

Without anatomical verification for the eye patch experiments, we are currently unable to conclude whether the three types of binocularity patterns recorded in this study pertain to specific TSDN types, so this possibility remains to be investigated. However, we do know that the extent of binocular overlap can change dramatically within a TSDN type across animals (Figure 4) and that simultaneously recorded TSDNs in the same animal exhibit different binocularity patterns (Figure 6A), evidencing that differences in binocularity are present within an individual and across the population. Our results suggest that such differences could arise from changes in eye dominance (weighing of inputs) and sensitivity (threshold). Changes in eye dominance can result from experience driven plasticity [44]. Since dragonfly TSDNs remain silent for the first 1-2 days after eclosion (Olberg, unpublished results), input weightings may be fine-tuned during this period. With regards to differences in threshold sensitivity, it is known that the same TSDNs recorded in different individuals of the same dragonfly species exhibit markedly different spiking levels [11], a finding reproduced here in demoiselles (Figure 4). This is likely a combination of recent stimulus history (repeated stimulation quickly results in a reduction of responses due to habituation), and internal state (such as hunger, temperature, or maturity level). Indeed, in the stomatogastric system of crabs and lobsters, the properties of individual neurons forming a circuit varies across animals, but all populations reach an equilibrium that produces a common motor output [45,46].

Whilst demoiselle TSDN receptive fields are binocular and receive bilateral input, our monocular (Figures 5-6A), and prism experiments (Figure 6B) indicate that the visual midline is nonetheless encoded within the inputs to these neurons. It is not clear from our data how a binocular TSDN threshold becomes positioned at the visual midline to yield the truncated Type 2 and Type 3 monocular receptive fields (Figures 5-6B). It is possible that interocular inhibition may be at play to fine tune the positioning of this threshold. Indeed, in the dragonfly lobula, heterolateral inhibitory feedback between centrifugal CSTMDs results in an abrupt decrease in firing rate as a target crosses the midline from the ipsilateral into the contralateral visual hemisphere [17,47]. Analogous circuitry in the demoiselle lobula may function to define a visual midline which could feed into threshold tuning.

In summary, we have presented evidence that target tracking information at the pre-motor level is fused across visual hemispheres in demoiselles. Binocular fusion is known to confer perceptual advantages relevant for a target tracking system such as enhanced visual sensitivity [2,3] and decreased reaction times [4]. However, such binocular fusion necessitates encoding visual motion in a binocular-fused frame of reference. In contrast, the reference frame of holoptic eyes is relative to the midline. This may result in a simpler descending control system that only needs to implement the commands from one eye/neuron, preventing the temporal resolution problems that may arise when integrating equivalent signals from neurons with different sensitives and latencies. As a trade-off, the holoptic eye is limited in stereoscopic computation of depth compared to a dichoptic morphology. Our data indicates that demoiselle TSDNs are disrupted when their binocular overlap is reduced by more than 10˚. It remains to be shown if these binocular neurons respond to disparities and whether a population of disparity tuned cells, which could be used for stereoscopic processing of depth, are present earlier in the demoiselle visual system.

Acknowledgments

This work was funded by the Air Force Office of Scientific Research (FA9550-15-1-0188 to PTGB and Karin Nordström, and FA9550-18-1-0339 to PTGB and TJW) and the Biotechnology and Biological Sciences Research Council (grant number BB/M011194/1 to JAS and BB/L024667/1 to TJW). This work was also supported by funding from the University of Minnesota College of Biological Sciences to PTGB and TJW. We thank Andrea Worthington for crucial support during the intracellular recording experiments; Francis Velasquez for his continuous logistic support; staff at Nixon Park for supporting fieldwork; York College for kindly providing us access to their facilities, and the University of Minnesota Insect collection for kindly allowing access to Odonata specimens. Special thanks to Mary Sumner for help with rearing damselflies and dragonflies in the lab, and to Abril K. Bellido-Wardill for her help during the dragonfly behavioural experiments.

Author Contributions

JAS, CK, TJW, and PTGB designed the study. JAS, STF, ML, DG, and SP collected behavioural data. JAS and SP analysed the behavioural data. JAS and DPB carried out the extracellular experiments and analysed the data. PTGB and RMO carried out the intracellular recordings, and RMO and JAS analysed the data. JAS, TJW, and PTGB processed and imaged the brain samples. HP and YW developed tools for neuron reconstruction and profiling. HP and LL managed the generation of reconstructions of JP and SJ, and performed the proofreading. JAS and PTGB wrote the first draft.

Declaration of Interests

The authors declare no competing interests.

Main text figure Legends

Figure 1 Comparison of external eye anatomy and hunting strategies of dragonflies and damselflies

(A) Frontal and lateral views of a dragonfly with holoptic eyes (*Sympetrum vulgatum*) and a demoiselle damselfly with dichoptic eyes (*Calopteryx splendens*). Yellow lines indicate visual area sampled by the dorsal (~60º elevated in dragonflies [10]) and frontal foveae, respectively. (B) Predatory flights of a dragonfly (i, *Erythemis simplicicollis*, Figure S1B, Video S1) and demoiselle (ii, *Calopteryx aequabilis*, Figure S1C, Video S2) whilst chasing an artificial prey (blue) reconstructed in 3D. Predator head positions are represented as a continuous red curve, with the body axis plotted at 10 ms intervals to indicate orientation of the predator throughout the attack (red lines). Line-of-sight between predator head position and artificial prey in grey. (C) Spherical plots, tracing the average subtended position of the prey (blue) compared to the body axis of the predator throughout the flight (red). Cones depict the 95% confidence interval of the prey just before the predator's first movement. In dragonfly attacks, the prey (dark blue) was on average aligned above the dragonfly body axis by 32.6° just prior to the first movement of the predator (95% CI = ± 12.4°, n=8) and by 33.7° throughout flight (95% CI = ± 5.3°, n=8). In demoiselle attacks, the prey (light blue) was on average aligned above the body axis by 13.9° just prior the first movement of the predator (95% CI = ± 13.0°, n=10) and by 11.4° throughout flight (95% CI = ± 6.5°, n=10). D=Dorsal, V=Ventral, A=Anterior, P=Posterior, L=Left, R=Right.

Figure 2 Target Selective Descending Neurons (TSDNs) in damselflies

(A) In damselflies there is a ventral shift relative to dragonflies in the receptive field of target responses recorded from the ventral nerve cord (see Figure S2A). Apart from this elevation difference, the color wheel used to encode direction is equivalent in both animals in keeping with the coordinate system used in [11]. (B) Set up and stimulus presented when recording target responses extracellularly from a demoiselle ventral nerve cord. Visual stimuli are comprised of 3000 target trajectories with random motion direction and start location, but fixed size and velocity, as used in dragonflies [11], allowing for comparative analysis. Top trace = raw responses to 44 trajectories indicated by steps on the stimulus trace (middle). Bottom trace: responses to a single target

trajectory where a target appears and remains stationary on the screen for 150 ms (red), moves with constant velocity (i.e. direction and speed) for 100 ms (green), and disappears for 150ms (grey) before the start of the next trajectory. The raster plot shows a subset of responses used to map the cell's receptive field (time is measured from stimulus onset). Further details for the analysis workflow are shown in Figures S2C and S3A-B. (C) Comparison between the receptive field maps of TSDNs in dragonflies and demoiselle TSDNs. All dragonfly maps were intracellularly acquired, and are here reproduced from [11]. The damselfly recordings, both extracellular and intracellular, show one recording (for all extracellular recordings see Figure S3C). The direction receptive field (RF) shows the position and direction of the target that elicited the spike. The spike triggered average (STA) displays the relative spiking activity across the receptive field, normalized to maximum number of spikes in that recoding in any one screen location (pixel). Polar histograms represent the binned target direction for each spike (10^o bins, black bars) and the resultant vector (red arrow) for the example receptive field. The red dots indicate the resultant vector direction for all neurons recorded. Elevation and azimuth scale are relative to the animal's head axis. The different types of TSDNs are labelled with their names (i.e. MDT1-5, DIT1-3). The symbol * next to a map notes that it was acquired intracellularly.

Figure 3 The TSDN Selective Descending Neurons (TSDNs) in damselflies and dragonflies are homologous.

TSDN traces of the damselfly neurons whose intracellular maps are shown in Figure 2, shown in comparison with the traces of TSDNs in Aeshnid dragonflies (reproduced with permission from [13,20]). The raw maximum intensity projection data, and the corresponding traces are shown for each cell in Video S3, the full 3D views are shown in Video S4. A= anterior, D= dorsal, V = ventral, L= left, R = right. In addition, see Figure S4 for details about a possible new type of TSDN, found in damselflies.

Figure 4 Spike number and degree of binocular overlap, within the same type of TSDNs, shows high variability between damselfly individuals.

We used the directional tuning (from electrophysiology) and the neuronal morphology (from dye fills) to identify that we had recorded from (A) MDT3 and (B) DIT1 in two and three animals, respectively. The high variability in spike numbers, and in the binocular overlap for each of these two TSDN types can be appreciated in such maps. Note that MDT3 was so named because it travels through the MDT track in Aeshnid dragonflies [13], but it travels though the DIT track in Libellulids [11], and in demoiselles (this study).

Figure 5 Demoiselle TSDNs are all binocular, with differing thresholds and input weights.

TSDNs were mapped under binocular (equivalent to Figure 2), and monocular conditions (left and right eye patches, in random order), followed by another binocular map as a

control. Monocular responses were categorized into three types (Types 1-3, A-C respectively), according to the binocular interaction observed. For each response type: row 1 = representative direction receptive field map from a single cell (example). Row 2 = average spike triggered map from cells falling within the category. Row 3 = relative response densities (STAs projected onto the horizontal axis, mean ± std for each cell recording). Row 4 = left vs right hemifield relative response cumulative sum. Row 5 = proposed summation-to-threshold model that could generate the responses. Full data given in Figure S5B. (A) Type 1 - Binocular-only, in which visual responses are dependent on both eyes in an all-or-none fashion. n = 3 cells allocated to this category. (B) Type 2 - Balanced split-monocular, in which receptive fields are bisected along the midline with absent responses from the hemifield ipsilateral to the eyepatch, and reduced responses, but still present, in the contralateral hemifield (arising from non-occluded eye). n = 4 cells allocated to this category. † For 1 cell, the right eye hemifield of this second control had an unusually high relative response. This hemifield was noted as an outlier, possibly caused by electrode or animal movement, and excluded from mean/variance calculation. (C) Type 3 - Ocular dominant, in which occlusion of one eye fully suppresses the entire receptive field. However, occlusion of the adjacent eye bisects the receptive field at the midline with responses found only in the non-occluded hemifield. n= 5 cells allocated to this category. †† One Type 3 cell is missing the uncovered positive control due to deterioration of recording signal (see Figure S5B).

Figure 6 Demoiselle TSDN receptive fields under opaque vs translucent eyepatches, and prisms

(A) The effect of global intensity on the TSDNs responses was tested by mapping them with opaque (as in Figure 2) and translucent eye patches (noted with letters O and T, see also Figure S6A-B). All three types of response categories described in Figure 2 were also found in this experiment. Receptive fields were recorded in series (i.e. binocular uncovered, left/right opaque eyepatch, binocular uncovered, left/right translucent eyepatch, binocular uncovered - the final binocular uncovered condition is excluded for presentation clarity). (B) A 4˚ and a 10˚ prism was used to test the TSDN responses under reduced binocular overlap between the two eyes (base out over left eye, producing deviation towards the left, Figure S6C). Reducing binocularity by 4˚ did not significantly affect spike density (two-sided sign test for matched pairs, $p = 1.0$, $n = 9$, blue traces), but a shift of 10˚ significantly lowered the spike densities compared to uncovered control (two-sided sign test for matched pairs, $p = 0.0078$, $n = 8$, see purple traces). No prism, or prism over both eyes served as controls for the effect of the prism. Rows 1 and 3 = three example directional receptive fields at each prism deviation. White arrowheads mark the right-hand boundary of the receptive field. White ellipses indicate the left-hand boundary of the receptive field. Rows 2 and 4 = Relative response densities (STAs projected onto the horizontal axis, mean ± individual traces from each recording, 4^o n=9 cells from 6 animals, 10^o n = 8 cells from 7 animals). Row 5 = Δ-Relative response plots calculated by subtracting the first binocular uncovered response density (control) from each condition. U=Uncovered; L=Monocular prism over left eye; B=Binocular Prism; U'=Uncovered control. Full data set for prism experiments in Figure S6D.

STAR★Methods

LEAD CONTACT AND MATERIALS AVAILABILITY

The lead contact for this article is Paloma Gonzalez-Bellido, paloma@umn.edu. This study did not generate new unique reagents.

EXPERIMENTAL MODEL AND SUBJECT DETAILS

Animals

Adult *Calopteryx splendens* were caught wild along the River Cam in Grantchester Meadows, Cambridge (UK), between May and August of years 2016-2018. *Calopteryx maculata* demoiselles were collected in York County, Pennsylvania (USA), during July 2017 and July 2019 with collection permission from park rangers. Between capture and experimentation, demoiselles were stored in humidified petri dishes to avoid desiccation. Animals were typically used for experiments on the day of capture; however, animals stored for longer periods were refrigerated to improve longevity and were used within 4-5 days maximum. *Erythemis simplicicollis* dragonflies were reared from nymphs (Carolina Biological Supply Company) in the lab, with adults maintained in an indoor flight arena feeding on *Drosophila melanogaster*.

METHOD DETAILS

High-speed Video Recordings videography of Predatory predation Behaviour

Two synchronised Photron SA2 cameras were used to film *Calopteryx maculata* demoiselles attacking artificial prey made from a silver 3 mm bead dangling on fishing line. The recordings were done either within a temporary outdoor plastic tent (York College) or unenclosed by a creek at Nixon State Park. *Erythemis simplicicollis* dragonflies hunting a black 3 mm bead were filmed using a similar dual synchronised Photron Mini AX200 camera system within an internal laboratory flight arena. High-

speed recordings were carried out at 1000 frames per second with either a 24 mm AF-S NIKKOR f/1.8G ED Nikon lens or a Nikon 85mm f/1.8D lens.

Behavioural Analysis

The dual image sequences from the synchronised camera systems were analysed off-line in MATLAB as previously described [S5,S6]. Briefly, the two-camera system was calibrated for 3D reconstruction based on a checkerboard calibration sequence using scripts originally written in J.Y. Bouguet's laboratory (Caltech, http://www.vision.caltech.edu/bouguetj/calib_doc/). For each video, the two synchronised image sequences were digitized in MATLAB to yield two (x,y)-coordinate time series for three points of interest: 1. position of the prey (bead), 2. the predator's head, and 3. the posterior tip of the predator's abdomen. These three stereo (x,y)-coordinate times-series pairs were then reconstructed into 3D cartesian space using the checkerboard calibration [S5,S6].

To trace the path of the prey relative to the predator's body axis during predatory flight, the body axis of the predator (digitised points 2 and 3, described above) from each frame of the recording were superimposed. Alignment assumed that the body axis did not rotate around the roll axis during flight (an assumption representative of Odonate flight, see videos S1-S2). Prey positions were reported relative to the aligned body axis, with positive angles representing dorsal elevations above the body azimuth.

The average elevation of the prey just prior to the flight initiation was calculated as follows: the frame prior to the predator's first movement was identified for each flight, the elevation values were measured (from the 3D flight reconstruction at each frame), and a circular mean from all flights was then calculated. The confidence interval for this measure is shown as the shaded cones in Figure 1C. To estimate the elevation of the prey relative to the head axis before take-off (estimation used in the discussion), the tilt angle between the body axis and the head axis was measured from macrophotographs (Figure S1D-E). The value of this offset was then applied to the elevation of the prey from body axis just prior to any movement of the predator.

The reported average and confidence intervals for the elevation of the prey, relative to the predator's body axis throughout flight, was calculated as follows: i. for each flight, an average elevation angle was calculated (i.e. circular mean of the values throughout a single trajectory) then, ii. the values obtained in (i) for each trajectory were averaged (i.e. circular mean of all the flights). The average trajectories shown as blue traces in Figure 1C were calculated as follows: i. normalising each trajectory to the maximum distance between the predator and prey throughout flight, ii. binning along 5% radial intervals (0% predator's head, 100% maximum distance of the prey), iii. averaging the elevation and azimuth values within each bin for each individual flight (circular mean within a bin), iv. averaging each bin across all flights (circular mean of bins across flights). Statistical tests reported in the main text were performed using the Watson-Williams test for equality of means.

Visual Stimuli

Visual stimuli were projected onto a 17.3 x 9.6 cm white screen using a DepthQ 360 projector (Cambridge Research Systems) with a spatial resolution of 1280 x 720 pixels running at 360 Hz, using StimulateOpenGL software (version 20160216, Janelia Research Campus, https://github.com/cculianu/StimulateOpenGL_II). Demoiselles were positioned 7 cm from the screen, giving a subtended projected screen size of 102 x 70 degrees. For initial receptive field mapping and monocular experiments, stimuli were chosen to match those described previously for comparison to Dragonflies [S4] . This stimulus consisted of a sequence of 3000 target trajectories, with each trajectory composed of three phases (Figure S2): (1) a small (2x2 degree) target appearing stationary at a random position on the screen for 150 ms before, (2) moving in a random direction for 100 ms at constant speed (160 degrees/s), followed by (3) a 150 ms delay before the next trajectory was presented. This method allows receptive fields to be mapped with high spatial resolution whilst avoiding fast habituation of the cell responses [S4].

A different mapping technique, with a lower number of trajectories, was designed to allow the opaque vs translucent vs prisms comparison of TSDN responses. In these experiments, the target stimulus scanned across the screen with longer trajectories, covering only eight directions (up/down/left/right

and diagonals). Target size and velocity was matched to the 3000 trajectory scans used in initial experiments (2x2 degree targets, 160 degrees/s velocity). Translucent eyepatches were made using electrical insulation film which strongly diffuses the light but are thin enough so as not to drastically reduce luminance (RS Components Ltd, product 536-3980; Figure S4). A 4˚ deviation (Newport, 25RB12-01UF.AR2) or 10˚ deviation Press-On-Prism (3M, 20 diopter. Cat# 90-12000) was positioned horizontally with the thinnest edge of the wedge positioned medial relative to the eye to avoid occluding the contralateral eye. This prism orientation results in a lateral shift of the visual field relative to the eye in monocular experiments.

Extracellular Electrophysiology Recordings

At experimental time, the animal was anaesthetised on ice, immobilized dorsal side down, and a small hole cut at the anterio-ventral thoracic surface to expose the ventral nerve cord. Extracellular recordings were performed as described previously (Nicholas et al., 2018). A sharp glass-insulated tungsten electrode (2-4 MOhm, Microelectrodes Ltd., Cambridge, UK) was inserted into the cervical connective, with mechanical support given to the cord by a small hook fashioned from a hypodermic needle. The animal was grounded using a saline-filled glass microelectrode inserted into the ventral cavity, which also served as the reference electrode (Fly saline as described in [S7]: 138 mM NaCl, 2 mM KCl, 1.8 mM $CaCl_2$, 4 mM $MgCl_2$, 5 mM TES, pH 7.15). Hydration of the ventral cavity was maintained by continual capillary action from an additional saline-filled glass microelectrode. Extracellular signals were amplified at 500x gain and filtered through a 300 – 3000 Hz analogue bandpass filter on an NPI BA-03x amplifier (NPI Electronic), filtered through a HumBug (Digitimer), digitized on a micro1401-3 DAQ (CED), and acquired at 25kHz with Spike2 software (CED). Measurements were taken at 23 °C. Typically 1, but sometimes up to 3 units were recorded, and typically between 0 to 2 were TSDN responses. TSDNs have, by far, the largest axons of the cord. Therefore, they have the largest probability of being picked up by the electrode.

Intracellular Electrophysiology Recordings

For intracellular recordings, the animals were prepared as described above for extracellular recordings. A metal spoon, made from a bent and polished needle, was then inserted into the cavity to ‘hug’ the

cord and provide support. Glass electrodes (thin wall borosilicate glass with an OD of 1 mm and ID of 0.75 mm; WPI Cat# TW100F–4) were pulled with a laser electrode puller (Sutter P-2000), by choosing the following settings: Heat 340; Fil 4; Vel 50; Del 210; Pul 150. Once the electrodes were filled with 1.5 or 3% Lucifer Yellow in 1M LiCl, or with 1M KCL, the resulting resistance was circa 80 or 20 MΩ, respectively. Negative current (total between -2 and -15 nA, depending on the preparation) was injected with square pulses (6 seconds on-1 second of), for as long as the cell was held, which was sometimes up to 1 hour. Measurements were taken at 23 °C. In total, 17 TSDN cells were recorded intracellularly and filled (experiments were carried out in 17 different animals).

Whole Brain Imaging

After dye filling the neurons, the animal was transferred to 4% paraformaldehyde overnight at room temperature. The day after, the preparation was washed with PBS, and the brain removed. The brain was then cleared following previous protocols [S8]. Cleared brains were positioned into a small groove of Sylgard (Sigma-Aldrich) submerged in 96% TDE (2,2′-thiodiethanol). Brains were imaged using an Olympus XLSL Plan N 25x /1.00 Glyc MP ∞/0-0.23/FN18 multiphoton objective, a Newport Spectra-Physics InSight® DS+™ laser at 920 nm, and a Bruker (Prairie Technologies) in vivo multiphoton microscope using GFP and RFP detection channels. Images were acquired as a tiled Z-stack at 0.9 μm isovoxel resolution (Prairie View v5.4), and stitched in Fiji [S9,S10]. Image stacks were converted into the TeraFly-compatible hierarchical representation and loaded into Vaa3D (http://vaa3d.org), with which the filled neurons were then traced [S11–S13]. For image regions with low signal-to-noise ratio (SNR) or containing complicated arborizations, TeraVR was adopted to achieve unambiguous tracing results [S13]. Each neuron reconstruction was produced by two annotators collaboratively for tracing and proofing using TeraVR and TeraFly tools, based on a standardized data production protocol developed by SEU-ALLEN Joint Center for the whole-mouse-brain full-neuron-morphology project (unpublished data).

QUANTIFICATION AND STATISTICAL ANALYSIS

Electrophysiology Analysis

Extracellular spike sorting was performed in Spike2 software (Cambridge Electronic Design Ltd, UK) using principal component analysis on waveform shapes followed by manual clustering. i.e. after the experiment was finished, the clusters of spikes in PCA space were manually circled and designated as a unit (Figure S2C). This was done with tools built in Spike2 software, for this purpose. Because the spike shape often changes gradually over time during the recording, the spike template could fit these gradual changes, and thus allocate the spikes as responses from the same neuron. However, if there was an abrupt change in spike shape, this was normally due to a sudden change in the location of the electrode (i.e. maybe due to animal movement), and thus, the spikes were not classified as belonging to the same unit. An acceptable clustering to the experimenter, looked like a cluster that was separated from all other spikes. This is a qualitative judgement in the spike sorting procedure and is not quantified in this study (see Figure S2C). Intracellular action potentials were detected with a manual threshold, with no further classification required. All further analysis was performed in MATLAB (Mathworks). For receptive field mapping in Figures 2-3, we calculated the latency for each cell. This latency (i.e. the time between stimulus presentation and the time at which the resulting spike was recorded in the connective), was used to identify the location and direction of the target that caused the spike (Figure S3A). Adjusting spike times by subtracting this latency gives a more accurate timestamp to correlate exactly where the target stimulus was in the visual field when the response was initiated [S4]. Direction field maps, direction histograms, and spike-triggered average (STA) maps were calculated as previously described [S4]. For eyepatch and prism experiments, raw STA maps were summed along the elevation axis yielding raw azimuth STA densities. Raw azimuth densities were smoothed and normalized to the maximum density value in the first uncovered condition. Relative response integrals were calculated as the sum of the normalized azimuth densities in each visual hemisphere. All spike count data is given as mean ± std. Δ relative response plots were calculated by subtracting the normalized relative response density of the first binocular (uncovered) control from that of all other conditions.

DATA AND CODE AVAILABILITY

All data generated was analysed during this study. All analyses are found within this published article. Raw data supporting the current study have not been deposited in a public repository because it is too large but are available from the corresponding author on request.

Supplemental video legends

Video S1. Dragonfly predatory attacks. Related to Figure 1.

Video S2. Demoiselle predatory attacks. Related to Figure 1.

Video S3. Anatomical tracing of intracellularly labelled demoiselle TSDNs. Related to Figure 3.

Video S4. 3D reconstructions of intracellularly labelled demoiselle TSDN. Related to Figure 3.

References

1. Barendregt, M., Harvey, B.M., Rokers, B., and Dumoulin, S.O. (2015). Transformation from a retinal to a cyclopean representation in human visual cortex. Curr. Biol. *25*, 1982–7.
2. Campbell, F.W., and Green, D.G. (1965). Monocular versus Binocular Visual Acuity. Nature *208*, 191–192.
3. Elberger, A.J. (1989). Binocularity and single cell acuity are related in striate cortex of corpus callosum sectioned and normal cats. Exp. brain Res. *77*, 213–6.
4. Blake, R., Martens, W., and Di Gianfilippo, A. (1980). Reaction time as a measure of binocular interaction in human vision. Invest. Ophthalmol. Vis. Sci. *19*, 930–41.
5. Ding, J., and Levi, D.M. (2011). Recovery of stereopsis through perceptual learning in human adults with abnormal binocular vision. Proc. Natl. Acad. Sci. U. S. A. *108*, E733-41.
6. Nityananda, V., and Read, J.C.A. (2017). Stereopsis in animals: evolution, function and mechanisms. J. Exp. Biol. *220*, 2502–2512.
7. Lythgoe, J.N. (1979). Ecology of Vision (Oxford University Press).
8. Grimaldi, D.A., and Engel, M.S. (2005). Evolution of the insects (Cambridge University Press).

9. Corbet, P.S. (1999). Dragonflies: Behaviour and Ecology of Odonata (Cornell University Press).

10. Olberg, R.M., Seaman, R.C., Coats, M.I., and Henry, A.F. (2007). Eye movements and target fixation during dragonfly prey-interception flights. J. Comp. Physiol. A *193*, 685–693.

11. Gonzalez-Bellido, P.T., Peng, H., Yang, J., Georgopoulos, A.P., and Olberg, R.M. (2013). Eight pairs of descending visual neurons in the dragonfly give wing motor centers accurate population vector of prey direction. Proc. Natl. Acad. Sci. *110*, 696–701.

12. Mischiati, M., Lin, H.-T., Herold, P., Imler, E., Olberg, R., and Leonardo, A. (2015). Internal models direct dragonfly interception steering. Nature *517*, 333–338.

13. Olberg, R.M. (1986). Identified target-selective visual interneurons descending from the dragonfly brain. J Comp Physiol A *159*, 827–840.

14. Olberg, R.M. (1981). Parallel Encoding of Direction of Wind, Head, Abdomen, and Visual Pattern Movement by Single Interneurons in the Dragonfly. J Comp Physiol J. Comp. Physiol. *142*, 27–41.

15. Lin, H.-T., and Leonardo, A. (2017). Heuristic Rules Underlying Dragonfly Prey Selection and Interception. Curr. Biol. *27*, 1124–1137.

16. O'Carroll, D. (1993). Feature-detecting neurons in dragonflies. Nature *362*, 541–543.

17. Wiederman, S.D., and O'Carroll, D.C. (2013). Selective Attention in an Insect Visual Neuron. Curr. Biol. *23*, 156–161.

18. Nordstrom, K., Bolzon, D.M., and O'Carroll, D.C. (2011). Spatial facilitation by a high-performance dragonfly target-detecting neuron. Biol. Lett. *7*, 588–592.

19. Perry, M.W., and Desplan, C. (2016). Love spots. Curr. Biol. *26*, R484–R485.

20. Frye, M.A., and Olberg, R.M. (1995). Visual receptive field properties of feature detecting neurons in the dragonfly. J. Comp. Physiol. A *177*, 569–576.

21. Olberg, R.C. (1978). Visual and multimodal interneurons in dragonflies. PhD thesis, Univ. Washingt.

22. Olberg, R.M. (1983). Identified interneurons steer flight in the dragonfly. Soc. Neurosci. Abstr. *9,326*.

23. Nel, A., Prokop, J., Pecharová, M., Engel, M.S., and Garrouste, R. (2018). Palaeozoic giant dragonflies were hawker predators. Sci. Rep. *8*, 12141.

24. Bechly, G., Brauckmann, C., Zessin, W., and Groning, E. (2001). New results concerning the morphology of the most ancient dragonflies (Insecta: Odonatoptera) from the Namurian of Hagen-Vorhalle (Germany). J. Zool. Syst. Evol. Res. *39*, 209–226.

25. Horridge, G.A. (1978). The Separation of Visual Axes in Apposition Compound Eyes. Philos. Trans. R. Soc. B Biol. Sci. *285*, 1–59.

26. von Reyn, C.R., Breads, P., Peek, M.Y., Zheng, G.Z., Williamson, W.R., Yee, A.L., Leonardo, A., and Card, G.M. (2014). A spike-timing mechanism for action selection. Nat. Neurosci. *17*, 962–970.

27. Rüppell, G. (1999). Prey capture flight of Calopteryx haemorrhoidalis (Vander Linden) (Zygoptera: Calopterygidae). Int. J. Odonatol. *2*, 123–131.

28. Ito, K., Shinomiya, K., Ito, M., Armstrong, J.D., Boyan, G., Hartenstein, V., Harzsch, S., Heisenberg, M., Homberg, U., Jenett, A., *et al.* (2014). A Systematic Nomenclature for the Insect Brain. Neuron *81*, 755–765.

29. Zhou, J., Clavagnier, S., and Hess, R.F. (2013). Short-term monocular deprivation strengthens the patched eye's contribution to binocular combination. J. Vis. *13*, 12–12.

30. Wakeling, J., and Ellington, C. (1997). Dragonfly flight. II. Velocities, accelerations and kinematics of flapping flight. J. Exp. Biol. *200*.

31. Walguarnery, J.W., Schröder, R., and Butler, M.A. (2009). Visual Target Detection in Damselflies. AFOSR grant Rep. *611102*.

32. Bidaye, S.S., Bockemühl, T., and Büschges, A. (2018). Six-legged walking in insects: how CPGs, peripheral feedback, and descending signals generate coordinated and adaptive motor rhythms. J. Neurophysiol. *119*, 459–475.

33. Labhart, T., and Nilsson, D.-E. (1995). The dorsal eye of the dragonfly Sympetrum: specializations for prey detection against the blue sky. J. Comp. Physiol. A *176*, 437–453.

34. Wardill, T.J., Fabian, S.T., Pettigrew, A.C., Stavenga, D.G., Nordström, K., and Gonzalez-Bellido, P.T. (2017). A Novel Interception Strategy in a Miniature Robber Fly with Extreme Visual Acuity. Curr. Biol. *27*, 854–859.

35. Barrós-Pita, J.C., and Maldonado, H. (1970). A fovea in the praying mantis eye. Z. Vgl. Physiol. *67*, 79–92.

36. Krapp, H.G., Hengstenberg, R., and Egelhaaf, M. (2001). Binocular Contributions to Optic Flow Processing in the Fly Visual System. J. Neurophysiol. *85*, 724–734.

37. Hennig, P., Kern, R., and Egelhaaf, M. (2011). Binocular Integration of Visual Information: A Model Study on Naturalistic Optic Flow Processing. Front. Neural Circuits *5*, 4.

38. Farrow, K., Haag, J., and Borst, A. (2006). Nonlinear, binocular interactions underlying flow field selectivity of a motion-sensitive neuron. Nat. Neurosci. *9*, 1312–1320.

39. Wertz, A., Borst, A., and Haag, J. (2008). Nonlinear integration of binocular optic flow by DNOVS2, a descending neuron of the fly. J. Neurosci. *28*, 3131–40.

40. Wertz, A., Haag, J., and Borst, A. (2009). Local and global motion preferences in descending neurons of the fly. J. Comp. Physiol. A *195*.

41. Huston, S.J., Krapp, H.G., Egelhaaf, M., Lindemann, J., and Egelhaaf, M. (2008). Visuomotor Transformation in the Fly Gaze Stabilization System. PLoS Biol. *6*, e173.

42. Scarano, F., Sztarker, J., Medan, V., Berón de Astrada, M., and Tomsic, D. (2018). Binocular neuronal processing of object motion in an arthropod. J. Neurosci. *38*, 6933–6948.

43. Rosner, R., von Hadeln, J., Tarawneh, G., and Read, J.C.A. (2019). A neuronal correlate of insect stereopsis. Nat. Commun. *10*, 2845.

44. Klink, P.C., Brascamp, J.W., Blake, R., and van Wezel, R.J.A. (2010). Experience-driven plasticity in binocular vision. Curr. Biol. *20*, 1464–9.

45. Marder, E., and Goaillard, J.-M. (2006). Variability, compensation and homeostasis in neuron and network function. Nat. Rev. Neurosci. *7*, 563–574.

46. Golowasch, J., Casey, M., Abbott, L.F., and Marder, E. (1999). Network Stability from Activity-Dependent Regulation of Neuronal Conductances. Neural Comput. *11*, 1079–1096.

47. Geurten, B.R.H., Nordström, K., Sprayberry, J.D.H., Bolzon, D.M., and O'Carroll, D.C. (2007). Neural mechanisms underlying target detection in a dragonfly centrifugal neuron. J. Exp. Biol. *210*, 3277–84.

KEY RESOURCES TABLE

REAGENT or RESOURCE	SOURCE	IDENTIFIER
Software		
MATLAB 2018, 2014, 2012, 2009	The Mathworks	MATLAB, RRID:SCR_001622
Python Programming Language	Python Software Foundation	RRID: SCR_008394
SciPy	http://SciPy.org	RRID: SCR_008058
StimulateOpenGL Version 20160216	Janelia Research Campus	StimulateOpenGL_II
FIJI	NIH	Fiji, RRID:SCR_002285
Vaa3D	HHMI, Allen Institute, and BrainTell (SEU-ALLEN)	Vaa3D, RRID:SCR_002609
TeraVR	BrainTell (SEU-ALLEN)	https://github.com/Vaa3D/release/releases/
TeraFly	BrainTell (SEU-ALLEN)	https://github.com/abria/TeraStitcher/wiki/TeraFly
Spike2 version 8	Cambridge Electronic Design	Spike2 Software, RRID:SCR_000903
Photron FASTCAM Viewer 3 Software (PFV3)	Photron	https://photron.com/software-downloads/
High Speed Videography Hardware		
Photron SA2 cameras	Photron	https://photron.com/fastcam-sa2/
Photron Mini AX200 cameras	Photron	https://photron.com/mini-ax/
24 mm AF-S NIKKOR f/1.8G ED Nikon lenses	Nikkon	https://www.nikonusa.com/en/nikon-products/product/camera-lenses/af-s-nikkor-24mm-f%252f1.8g-ed.html
85mm f/1.8D lens Nikon lenses		https://www.nikonusa.com/en/nikon-products/product-archive/camera-lenses/af-nikkor-85mm-f%252f1.8d.html
Electrophysiology Hardware		

NPI BA-03x amplifier	NPI Electronic	http://www.npielectronic.de/products/amplifiers/ba-bridge-amplifier/ba-03x.html
Humbug	Digitimer	https://digitimer.com/products/research-electrophysiology/hum-bug-noise-eliminator/hum-bug-ne/
Micro1401-3 DAQ	Cambridge Electronic Design	http://ced.co.uk/products/micro3
Tungsten Electrodes	Microelectrodes ltd.	www.microelectrodes.net,Tungsten 11-15 µm tip, 2-4MOhm impedance
Eyepatches and Prisms		
Electrical insulation film	RS Components Ltd	Cat# 536-3980
Wedge Prism 25RB12-01UF.AR2	Newport	https://www.newport.com/p/25RB12-01UF.AR2, Cat# 25RB12-01UF.AR2
10-degree Press-On-Prism (20 diopter)	3M	https://www.3m.com/3M/en_US/company-us/all-3m-products/~/3M-90-12000-PRESS-ON-Prism-20-00-Diopter/?N=5002385+3292952687&rt=rud, Cat# 90-12000)
2-Photon Microscopy		
In Vivo Ultima Multiphoton Microscope	Bruker	https://www.bruker.com/products/fluorescence-microscopes/ultima-multiphoton-microscopy.html
Spectra-Physics InSight® DS+™ laser	Newport	https://www.spectra-physics.com/products/ultrafast-lasers/insight-x3
Olympus XLSL Plan N 25x /1.00 Glyc MP ∞/0-0.23/FN18 Multiphoton Objective	Olympus	https://www.olympus-lifescience.com/en/objectives/multiphoton Cat# XLSLPLN25XGMP
Intracellular electrophysiology, dye loading and processing of dye filled brains		
Fixable Lucifer Yellow Dye	Invitrogen	https://www.thermofisher.com/order/catalog/product/L1177 Cat# L1177
Laser electrode puller	Sutter	Cat# P2000

Glass electrodes	World Precision Instruments	Cat# TW100F – 4, OD of 1 mm and ID of .75 mm, Heat 340; Fil 4; Vel 50; Del 210; Pul 150.
Anti-Lucifer Yellow antibody conjugated with biotin	Thermo Scientific	Thermo Fisher Scientific Cat# A-5751, RRID:AB_2536191
NeutrAvidin conjugated to DyLight 633,	Thermo Scientific	Cat# 22844, https://www.thermofisher.com/antibody/product/NeutrAvidin-Protein/22844
Collagenase/dispase	Sigma-Aldrich	Cat# 10269638001, https://www.sigmaaldrich.com/catalog/product/roche/colldispro?lang=en&region=US
Hyaluronidase	Sigma-Aldrich	Cat# H4272, https://www.sigmaaldrich.com/catalog/product/sigma/h4272?lang=en&region=US
Universal antibody dilution buffer	Electron Microscopy Sciences	Cat# 25885, https://www.emsdiasum.com/microscopy/technical/datasheet/25885.aspx
TDE	Sigma-Aldrich	99% 2,2′-Thiodiethanol, Cat# 166782, https://www.sigmaaldrich.com/catalog/product/aldrich/166782?lang=en&region=US

Figure 1

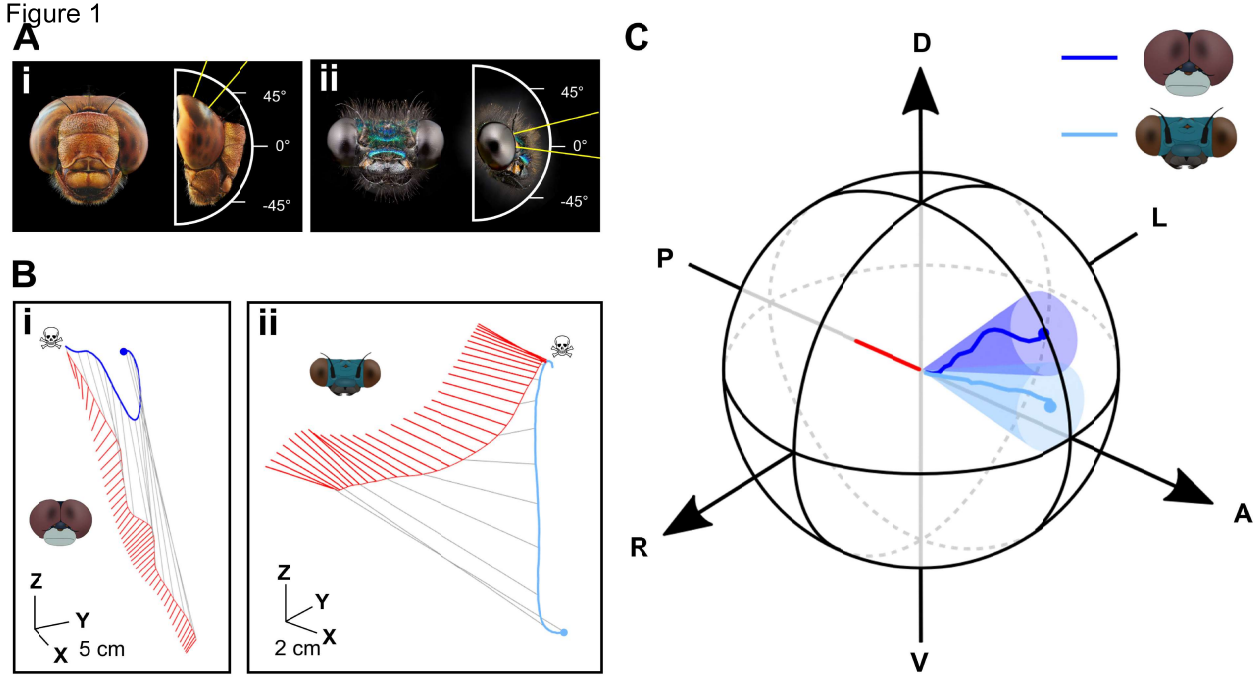

Figure 2

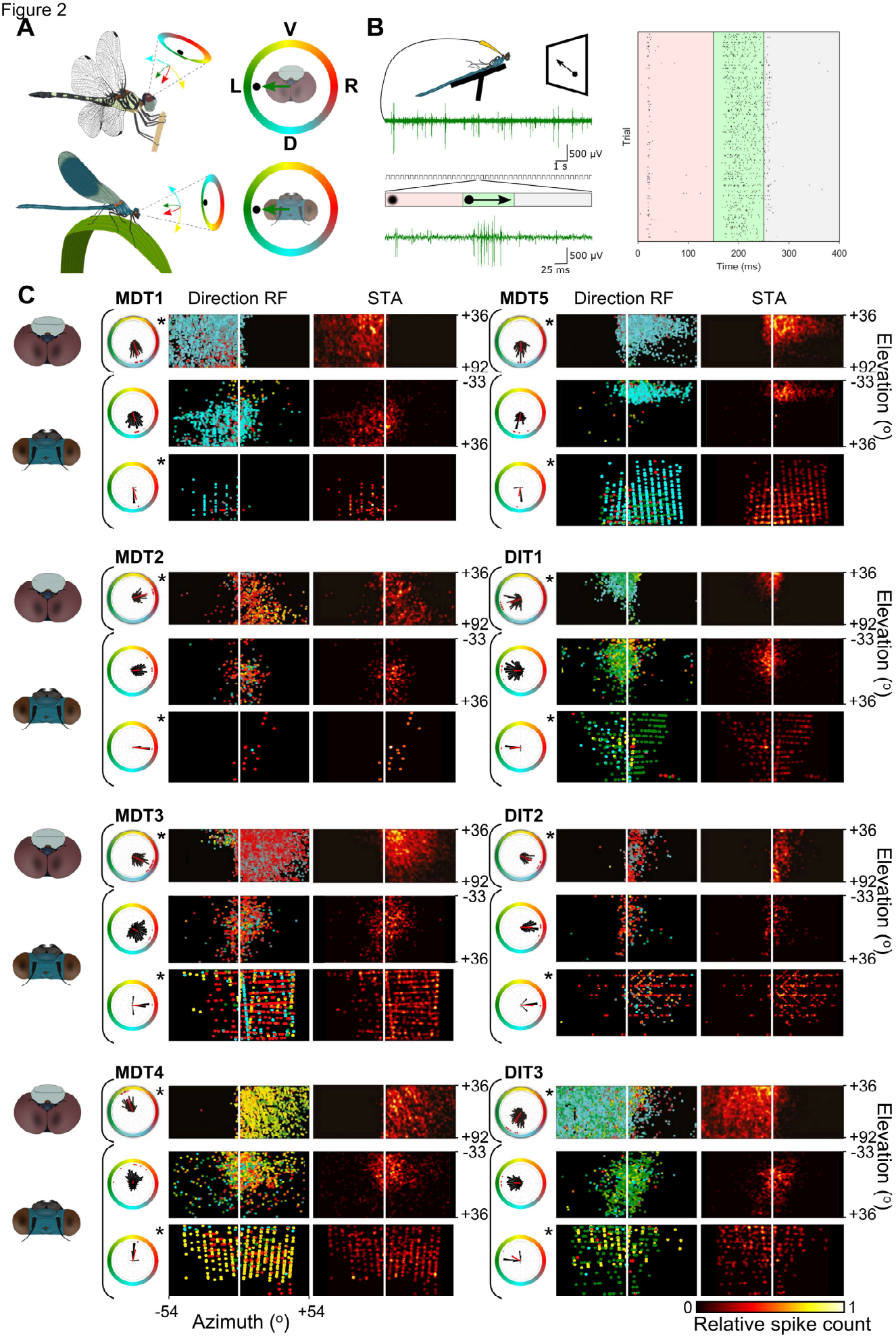
A
V
L
R
D
B
500 µV
1 s
500 µV
25 ms
Trial
0
100
200
300
400
Time (ms)
C
MDT1
Direction RF
STA
MDT5
Direction RF
STA
+36
+92
-33
+36
Elevation (°)
MDT2
DIT1
MDT3
DIT2
MDT4
DIT3
-54
Azimuth (°)
+54
0
1
Relative spike count

Figure 3

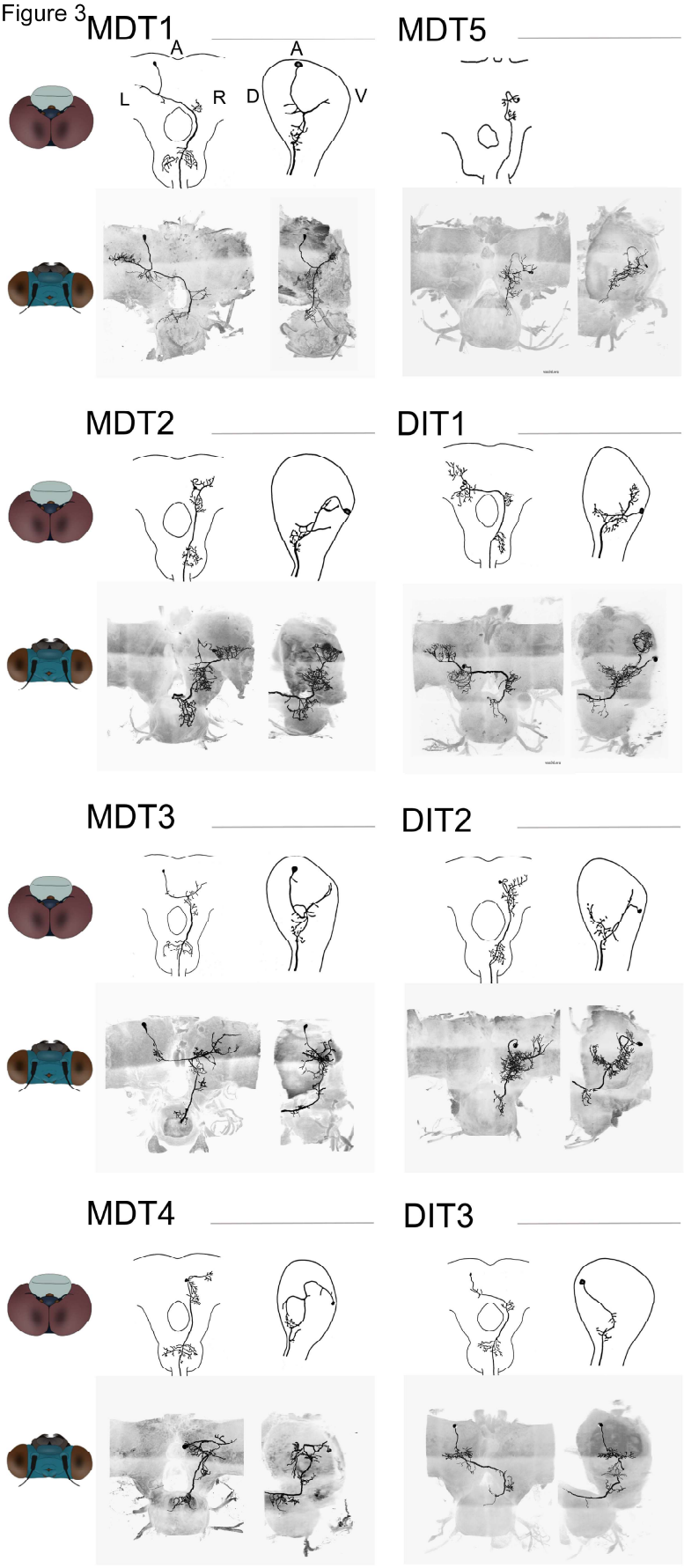

Figure 4

A

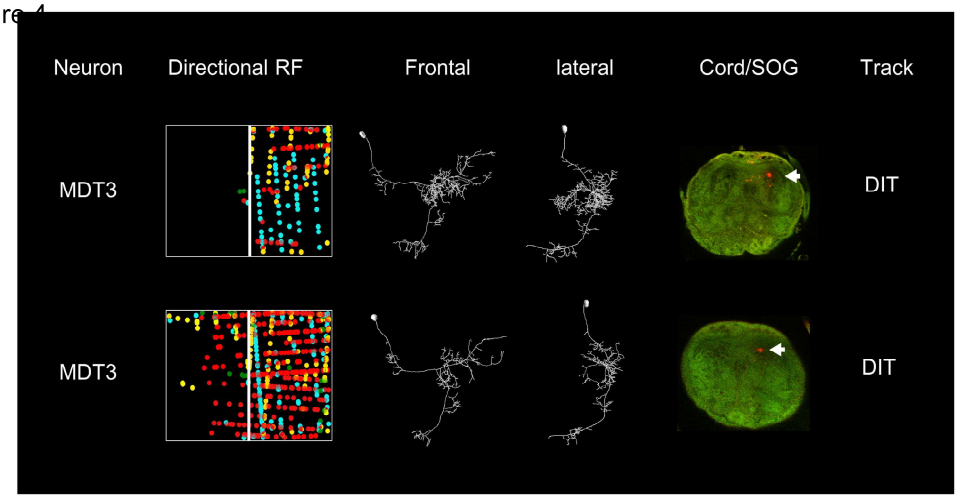
Neuron
Directional RF
Frontal
lateral
Cord/SOG
Track
MDT3
DIT
MDT3
DIT

B

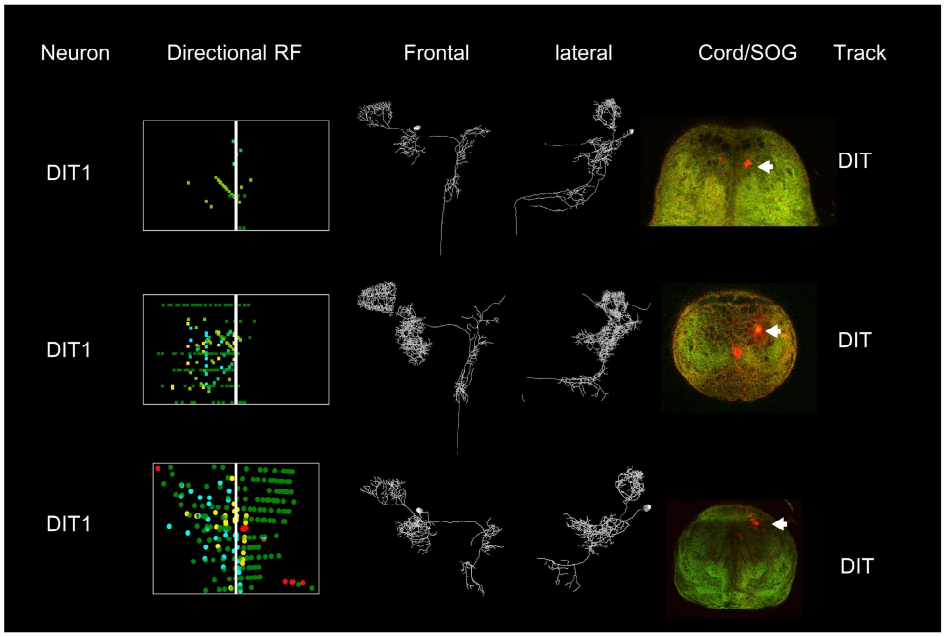
Neuron
Directional RF
Frontal
lateral
Cord/SOG
Track
DIT1
DIT
DIT1
DIT
DIT1
DIT

Figure 5

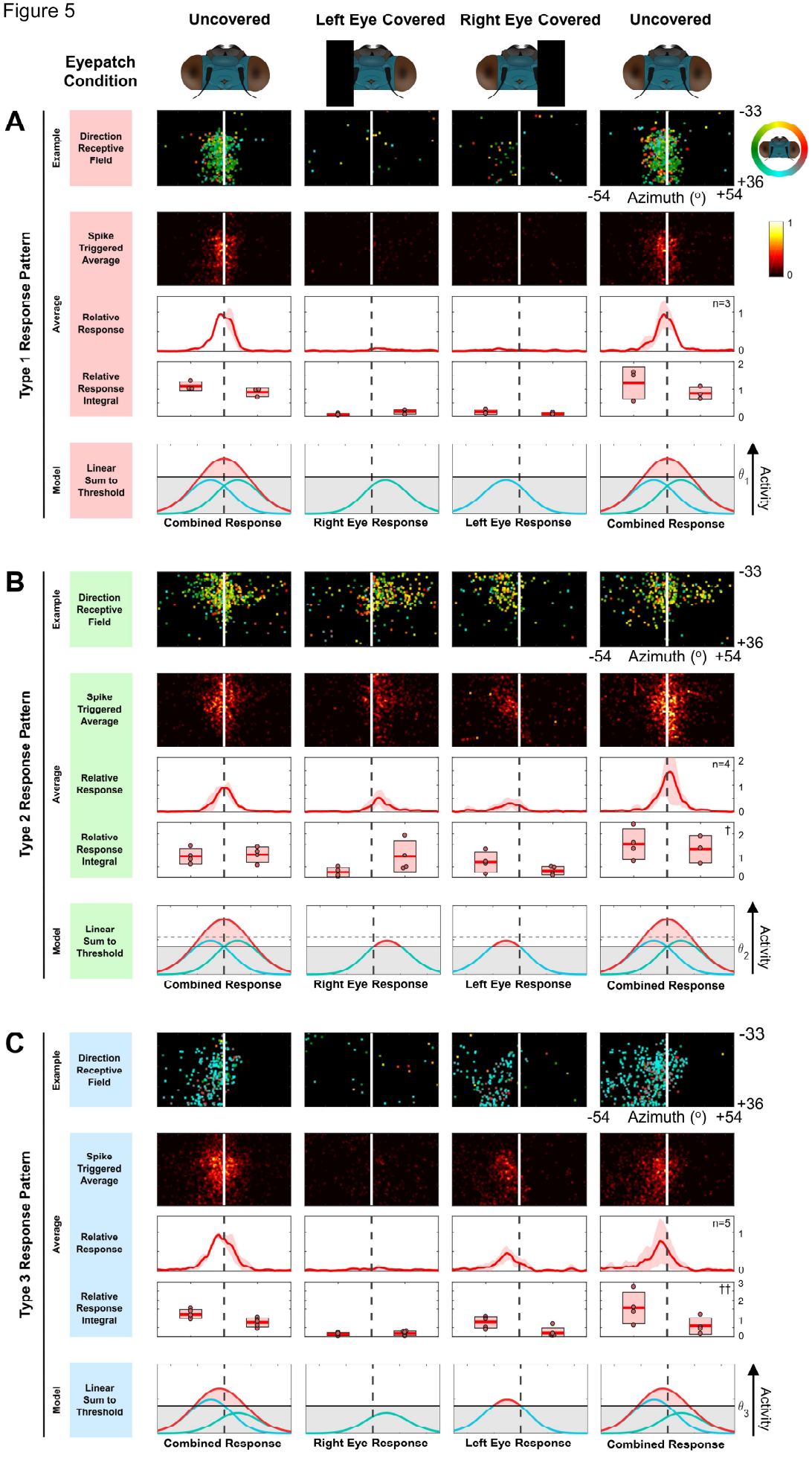
Uncovered
Left Eye Covered
Right Eye Covered
Uncovered
Eyepatch Condition
A
Type 1 Response Pattern
Example
Direction Receptive Field
-33
+36
-54
Azimuth (°)
+54
Average
Spike Triggered Average
Relative Response
n=3
Relative Response Integral
Model
Linear Sum to Threshold
Activity
Combined Response
Right Eye Response
Left Eye Response
Combined Response
B
Type 2 Response Pattern
n=4
†
C
Type 3 Response Pattern
n=5
††

Figure 6

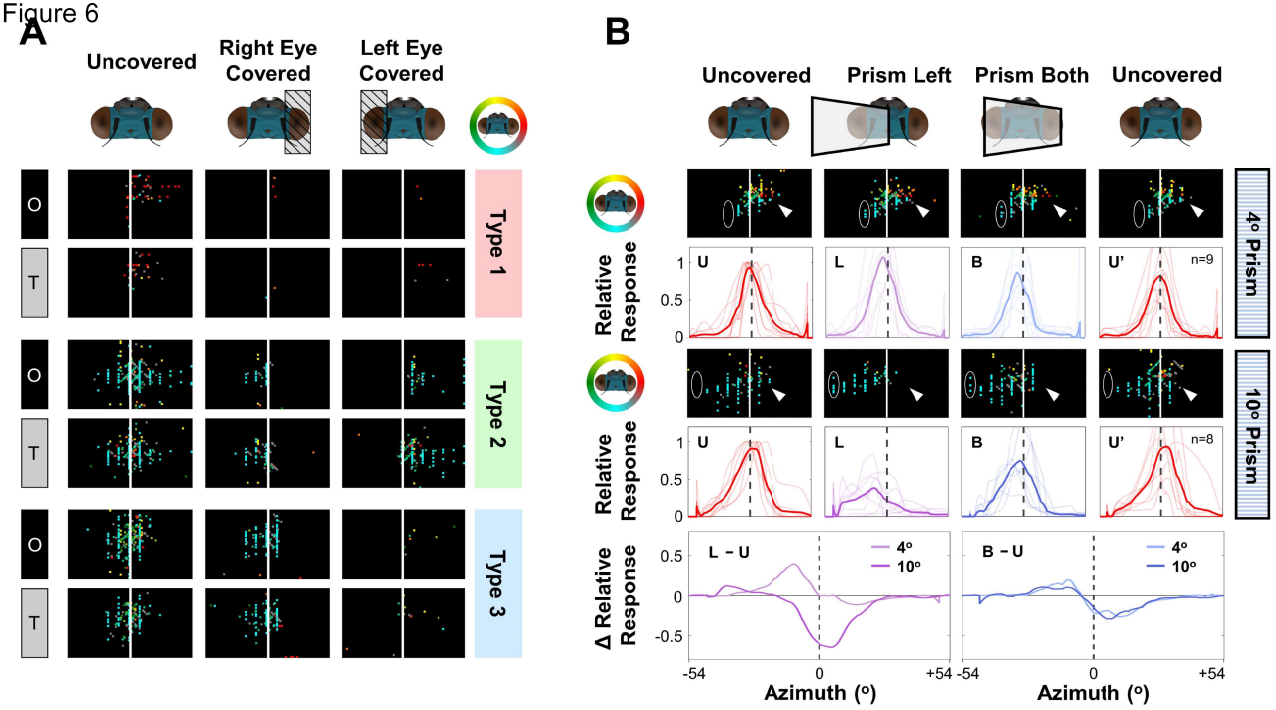
A
Uncovered
Right Eye Covered
Left Eye Covered
O
T
Type 1
Type 2
Type 3
B
Uncovered
Prism Left
Prism Both
Uncovered
4° Prism
10° Prism
Relative Response
U
L
B
U'
n=9
n=8
Δ Relative Response
L – U
B – U
4°
10°
Azimuth (°)
-54
0
+54

Supplemental Data

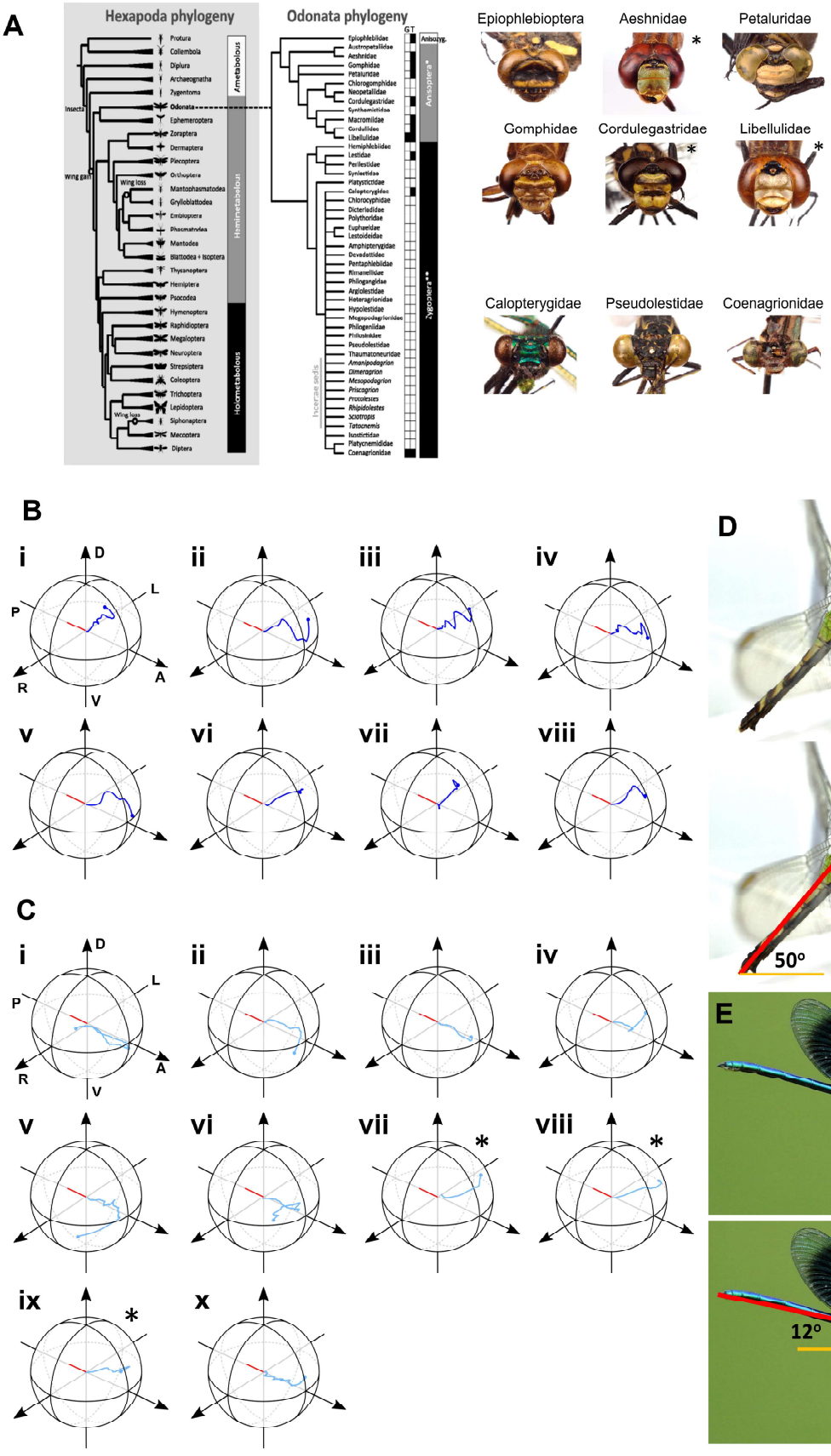

Figure S1 Odonata phylogeny with comparison of eye morphology, and predatory attack trajectories. Related to Figure 1.

(A) Odonatoptera phylogeny (left) reproduced from [S1] under a creative commons license (http://creativecommons.org/licenses/by/4.0/). Several extant dragonflies with holoptic morphology are indicated with asterisks (right). An ancient protodonatan 'griffenfly' has recently been discovered to also have possessed holoptic eyes [S2]. All other extant dragonflies, damselflies, and basal Odonatopterans [S3] feature dichoptic eyes. (B) Full dataset of dragonfly (i-viii) and (C) demoiselle (i-x) attack trajectories, tracing the path of the artificial prey relative to the body axis. D=Dorsal, V=Ventral, A=Anterior, P=Posterior, L=Left, R=Right. Data corresponds to that in Videos S1-2. Note that the three demoiselle trajectories marked with an asterisk show a more dorsal attack because the location of the bead was changed slowly around the animal from posterior-dorsal to anterior-ventral. Thus, the results of those trajectories aimed to identify the dorsal limit for the location of a bead that elicits a demoiselle attack. (D) Picture of an *Erythemis simplicicollis* dragonfly in hunting position in our arena, and the measurements of the differences in orientation between body and head axis in such conditions. The body axis and head axis are positioned 50º and 20º relative to the horizon, respectively. Thus, the head is tilted ventrally by 30º (50º – 20º) relative to the body axis when the animal is perched. (E) A picture of *Calopteryx splendens* in the wild (image credit, Dave Soons), and the measurements of the differences in orientation between body and head axis in such conditions. The body axis is tilted downward 12º degrees when perched, with the head axis aligned with the horizon. Thus, the head is tilted dorsally 12º relative to the body axis when the animal is perched.

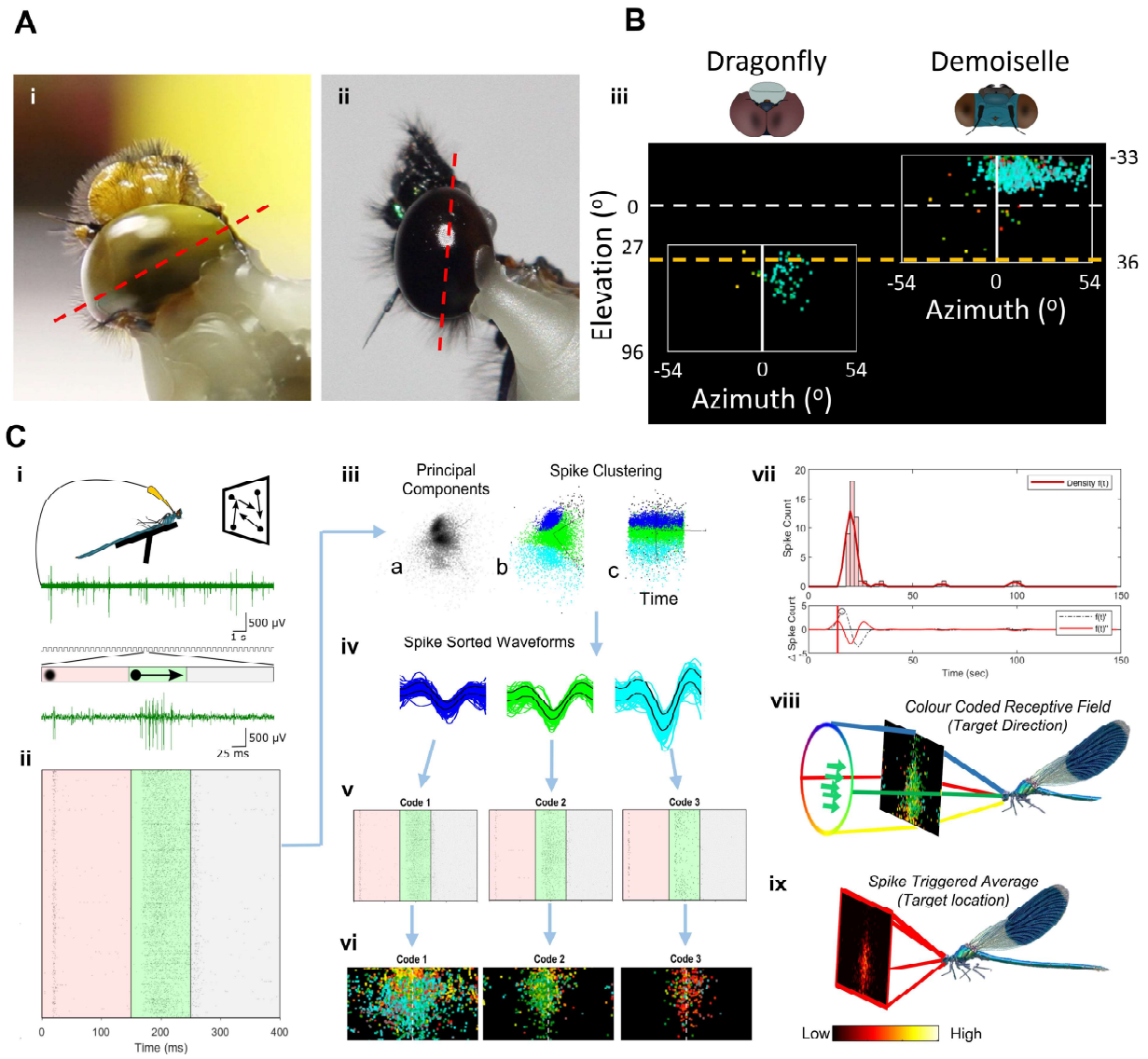

Figure S2 animal placement, preparation for electrophysiology. **Related to Figure 2**.

(A) We positioned animals so that the highest number of spikes to a moving bead around the animal would occur when the bead was in front of the projector screen. The elevation angle of the heads was different between dragonflies and damselflies. (B) We calculated the subtended location and size of our screen, relative to the fovea of the animal, from the geometry of our setup (i.e. distance between animals and screen, tilt of the animal's head, height of the animal's head, actual size of the screen. White dashed line indicates the head axis defined as 0°. Yellow dashed line indicates the dorsal-most aspect of the demoiselle receptive field mapped in our experimental setup. This indicates that the TSDN responses of damselflies occur more ventrally (relative to the head) than in dragonflies. (C) (i) Damselflies were positioned for extracellular recordings on a platform with the frontal aspect of the head positioned to view a screen onto which was projected a series of small target trajectories. Each trajectory consisted of a small target appearing stationary

at a random location on the screen for 100 ms (red phase), moving in a random direction at constant speed for 150 ms (green phase), then disappearing for 100 ms before the start of the next trajectory (grey phase). (ii) Extracellular ventral nerve cord spikes to 3000 of these trajectories are displayed as a raster plot. Demoiselle TSDNs respond with an ON-transient to object appearance, followed by activity throughout movement of the object. Spikes are detected using a manually adjusted spike-detection voltage threshold. (iii) The full set of detected spikes is then spike sorted into individual units using Principal Component Analysis (PCA) on spike waveform shapes followed by manual clustering. Clustering considers both the features in PCA space (iii-a-b), as well as the trajectory of a recorded neuron's spike waveform through PCA space over time (iii-c). The black points in (a) are individual spikes plotted proportional to the density of points in PCA space. Some areas of the data in (a) are darker than others indicating there are more spikes clustered closer together in these areas. Clustering is qualitative and falls to the subjectivity of the experimenter as follows. One can see two distinct dark blobs connected by a fainter area at the boundary, which would result from two individual distributions of spikes with the tails of the distributions overlapping. These are colored dark blue and green in (b). In addition to these two main blobs, there is a fainter distribution of sparser spikes at the bottom of (a), colored cyan in (b). This fainter distribution appears distinct from the main density directly above (green in (b)) due to the cinching (narrowing) of the data at the border of this fainter density and the main density above. Note that the density of the data looks different in (a) compared to (b-c) because the colored data is not presented as a scaled proportional density plot. This results in adjacent and superimposed color data points saturating the plot. (iv) Example spike sorted waveforms are shown, with colors corresponding to the clustered PCA features in (iii). (v) Raster plots for each spike sorted code using the same format as in (ii). (vi-vii) From each spike sorted raster plot, the spike latency (vii, See Figure S3) is calculated and subtracted from the spike sorted spike times before generating receptive field plots (vi) to more accurately determine what moment in the stimulus led to the generation of the recorded spike. (vii) Latency is defined as the moment when the peri-stimulus time histogram (PSTH, top panel) of the spike sorted raster plot starts to rise (indicated with the vertical red line) and is calculated as the time of the maximum peak in the second derivative (bottom panel, red curve) that precedes the maximum peak in the first derivative (bottom panel, black curve) of the PSTH (top panel). (viii) The calculated latencies are subtracted from the spike times, and the direction and location of the moving object in the visual field is recorded and plotted as a direction receptive field map. (ix) Responses are also displayed as a spike triggered average map to account for variations in relative spiking activity across the visual field.

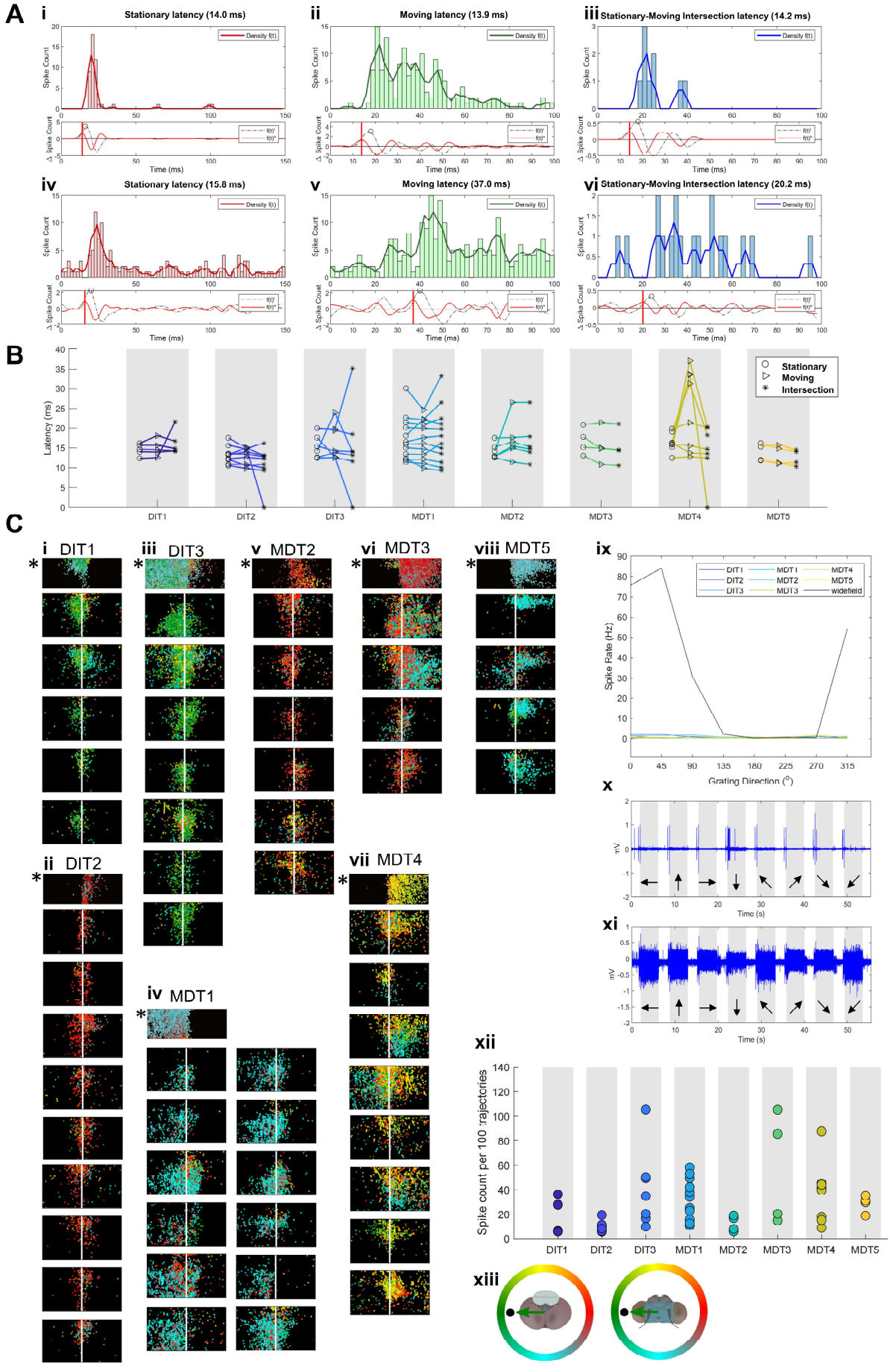
A
i Stationary latency (14.0 ms)
ii Moving latency (13.9 ms)
iii Stationary-Moving Intersection latency (14.2 ms)
iv Stationary latency (15.8 ms)
v Moving latency (37.0 ms)
vi Stationary-Moving Intersection latency (20.2 ms)
Density f(t)
Spike Count
Δ Spike Count
f(t)'
f(t)''
Time (ms)
B
Latency (ms)
Stationary
Moving
Intersection
DIT1
DIT2
DIT3
MDT1
MDT2
MDT3
MDT4
MDT5
C
i DIT1
ii DIT2
iii DIT3
iv MDT1
v MDT2
vi MDT3
vii MDT4
viii MDT5
ix
Spike Rate (Hz)
Grating Direction (°)
widefield
x
mV
Time (s)
xi
xii
Spike count per 100 trajectories
xiii

Figure S3 TSDN latencies and initial dataset of extracellular TSDN responses. Related to Figure 2.

(A) Latency calculations for stationary and moving objects. Top panels, peri-stimulus time histogram (PSTH) and density. Bottom panels, automated derivative latency calculation. The first derivative of the PSTH density (black line, f(t)') typically peaks within the main rising phase of spike onset from which latency is calculated. The peak of the second derivative (red line, f(t)'') is taken as the spike latency and represents the initiation of spike onset (vertical red line). (i-iii) Example of a recording where stationary (i) and moving phase latencies (ii) are approximately the same. (iv-vi) Example of a recording where the stationary (iv) and moving phase latencies (v) differ. This often arises from objects originating outside the receptive field of the neuron, and latencies appear longer as the object needs to move into the receptive field before spikes are initiated. This can be mitigated by only including trajectories with responses within both the stationary and moving phase (labelled 'stationary-moving intersection latency') (vi), although the number of spikes within this condition is often very low (compare y-axis range in iv-vi), which disrupts the automated latency calculation.

(B) Comparison of demoiselle TSDN latency measurements for stationary (circles), and moving phases (triangles), and trajectories that include both stationary and moving phase spikes (intersection, asterisks).

(C) The receptive field maps of demoiselle TSDNs are allocated qualitatively to TSDNs types known from dragonflies (dragonfly maps marked with an asterisk), according to their directional tuning, as well as size and center position of the receptive field. All recorded demoiselle TSDN receptive fields deemed to have acceptable spike sorting are included. The most difficult assignments were between dragonfly DIT1/DIT3 (i-ii) and DIT2/MDT2 (vi-vii) as the directional tuning of these cells is very similar. For DIT2/DIT3 (i-ii) the distinction was made by the vertical extent of the receptive field, with DIT3 (ii) having a longer vertical extent compared to DIT1 (i) in dragonflies. For DIT2/MDT2 (vi-vii), the distinction was based on the horizontal extend of the receptive fields, with dragonfly MDT2 (vii) having a wider horizontal spread in the receptive field compared to DIT2 (vi). (ix) Responses of all demoiselle TSDN types to widefield moving gratings, compared with responses from a widefield detecting neuron. (x) Example demoiselle TSDN response to widefield grating stimuli (grey). The neuron (blue trace) responds when the stimulus is loaded due to an off-on flicker between stimuli, but the neuron does not respond with sustained activity during grating movement (grey). (xi) Example demoiselle widefield neuron responding to the same widefield gratings (grey). (xii) Spike counts per 100 trajectories for each demoiselle TSDN receptive field in (i-viii). Demoiselle TSDN spike counts fall within a similar range to dragonfly TSDNs [S4], falling between 5 – 105 spikes per 100 trajectories. (xiii) Dragonfly and damselfly coordinate systems for the direction receptive field plots in (i-xiii).

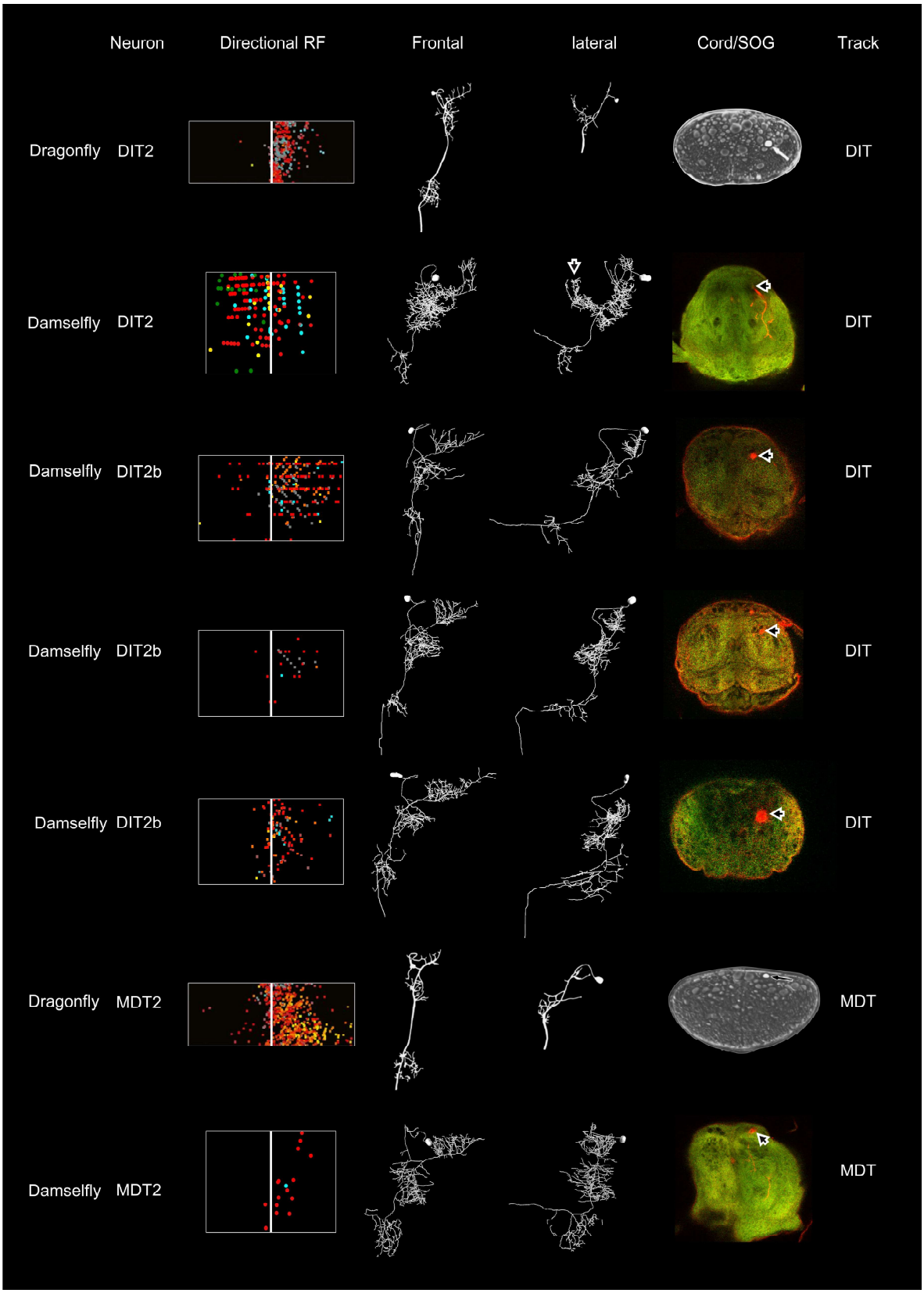
Neuron
Directional RF
Frontal
lateral
Cord/SOG
Track
Dragonfly DIT2
DIT
Damselfly DIT2
DIT
Damselfly DIT2b
DIT
Damselfly DIT2b
DIT
Damselfly DIT2b
DIT
Dragonfly MDT2
MDT
Damselfly MDT2
MDT

Figure S4 DIT2-b, possibly a new type of TSDNs. Related to Figure 3.

Both in dragonflies and damselflies, DIT2 is distinguished from other TSDNs by an ipsilateral morphology, an axon that travels through the DIT track, and directional preference toward the lateral of the animal. (i.e. red in our plotting system when recording this neuron from the right side of the cord). As their names suggests, DIT2 can be distinguished from MDT2 by the tracks that their axons travel in. In damselflies, we have recorded and labelled three cells, which appear to be the same type of TSDN, but do not completely match DIT2 or MDT2. These cells run through the DIT2 track but lack the posterior branch that is so prominent in DIT2 (white edge arrow in lateral projection). Given that the branching pattern of MDT2 resembles that of DIT2 without a posterior branch (Figure S4), it is possible these neurons were MDT2 that happened to travel through the DIT track in different individuals. This is unlikely given the otherwise highly conserved tract allocation of other TSDN types across individuals within a species. Alternatively, it is possible that the missing posterior branch resulted from incomplete fluorescent labelling; however, the posterior branch is very large, and its absence was observed in several specimens with otherwise high-quality dendritic labelling. Provisionally, and until further evidence refutes the existence of an additional TSDN type, we have termed these cells DIT2-b. White-edge arrow in track columns point to the profile of the filled neuron, as the cord enters the SOG (in demoiselle) or in the ventral cord (dragonflies). Dragonfly data reproduced from [S4].

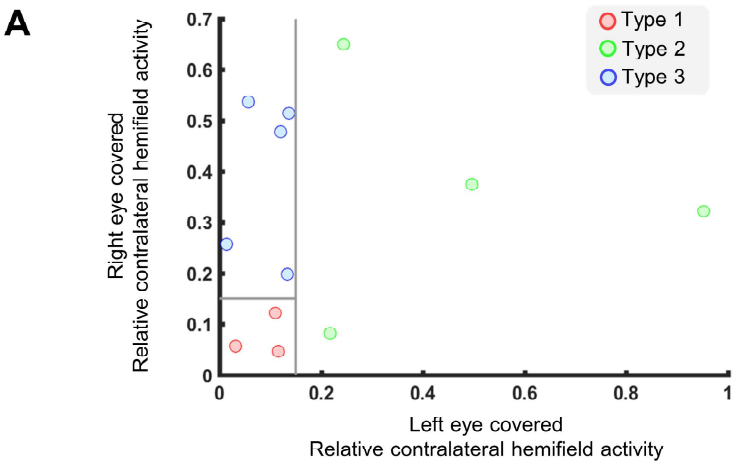
A
Type 1
Type 2
Type 3
Right eye covered
Relative contralateral hemifield activity
0.7
0.6
0.5
0.4
0.3
0.2
0.1
0
0
0.2
0.4
0.6
0.8
1
Left eye covered
Relative contralateral hemifield activity

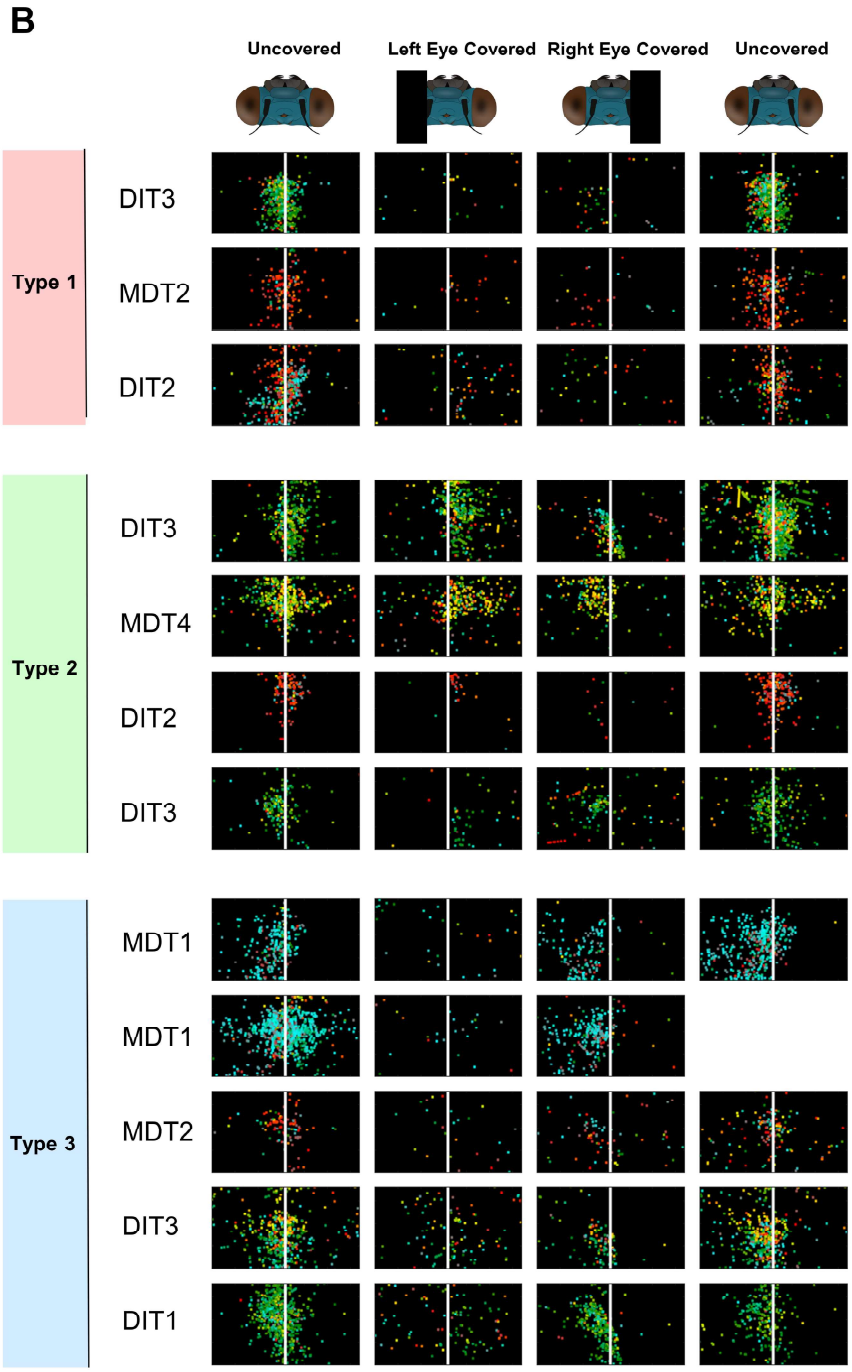
B
Uncovered
Left Eye Covered
Right Eye Covered
Uncovered
Type 1
DIT3
MDT2
DIT2
Type 2
DIT3
MDT4
DIT2
DIT3
Type 3
MDT1
MDT1
MDT2
DIT3
DIT1

Figure S5 Maps of TSDNs tested under opaque eyepatch conditions. Related to Figure 5.

(A) The measure used to allocate TSDNs to Type 1, 2 or 3 binocular responses is shown here. TSDNs with contralateral relative activity to the patched eye below 0.15 in both eyes formed response Type 1 (red). Type 2 responses was composed by TSDNs whose activity in the hemifield contralateral to the covered left eye was > 0.15 (green). Type 3 responses were those where the activity of the contralateral eye was < 0.15 if the left eye was patched, but >0.15 when the right eye was patched. (B) Original directional receptive field maps, and their putative TSDN IDs, resulting from the opaque eye patch experiment. These data were used to calculate averages shown in Figure 5. Monocular conditions are with the opaque eyepatch. The spike counts of these receptive fields were each normalized to the maximum pixel spike count in the first binocular uncovered condition. These normalized receptive fields were then averaged to form the data in Figure 3. Suggested TSDN ID is shown on the left.

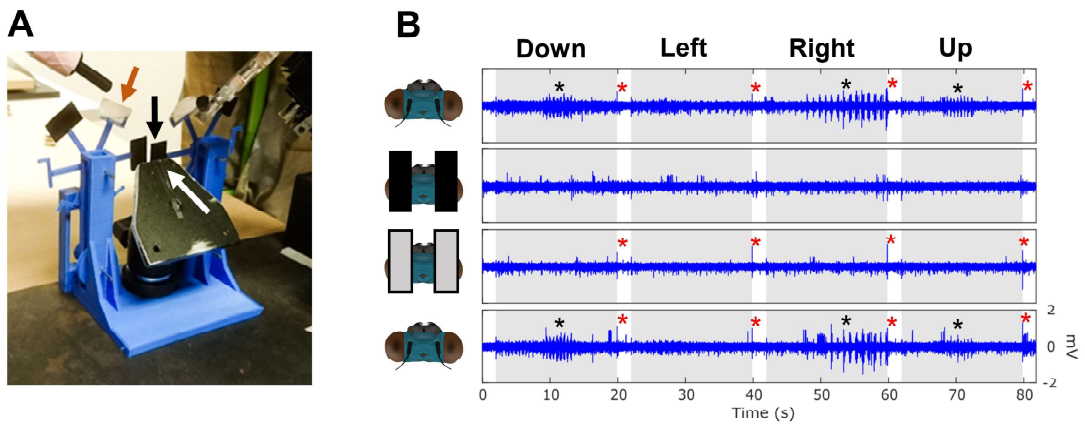
A
B
Down
Left
Right
Up
2
0
-2
mV
0
10
20
30
40
50
60
70
80
Time (s)
C
Prism over left eye only test
Screen
θ
Prism
Prism over both eyes control
Screen
θ
θ
D
Uncovered
Prism Left
Prism Both
Uncovered
i
4° Prism
ii
Uncovered
Prism Left
Prism Both
Uncovered
10° Prism

Figure S6 Maps of TSDNs tested with opaque vs translucent eyepatches, and with prisms. Related to Figure 6.

(A) 3-D printed eyepatch machine (blue) used to position eyepatches made from different materials independently in front of each eye. White arrow - platform to position animal; Orange arrow - translucent eyepatch; Black arrow - opaque eyepatch. (B) Ventral nerve cord responses to small targets scanning across the visual field along four directions under uncovered (first and last rows), binocular opaque (second row), and binocular translucent eyepatches (third row). Responses present in both uncovered conditions (black asterisks) were abolished when both eyes were covered with either the opaque (second row) or translucent eyepatches (third row). Under both uncovered (first and last rows) and translucent eyepatch (third row) conditions there was a transient 'off' response (red asterisk) at the end of each stimulus (grey blocks) which correlates with a step decrease in screen intensity when the stimulus finishes rendering. This transient off response was not present under opaque eyepatch conditions. (C) Putting a wedge prism, base out, in front of the left eye reduces the binocular overlap between the two eyes by the deviation induced by the prism. Putting the wedge prism in front of both eyes simply shifts the entire visual field leftwards, and thus acts as a control. (D) Entire data set for the electrophysiological responses of TSDNs tested with 4˚ and 10˚ prisms.

SUPPLEMENTAL REFERENCES

S1. Bybee, S., Córdoba-Aguilar, A., Duryea, M.C., Futahashi, R., Hansson, B., Lorenzo-Carballa, M.O., Schilder, R., Stoks, R., Suvorov, A., Svensson, E.I., *et al.* (2016). Odonata (dragonflies and damselflies) as a bridge between ecology and evolutionary genomics. Front. Zool. *13*, 46.

S2. Nel, A., Prokop, J., Pecharová, M., Engel, M.S., and Garrouste, R. (2018). Palaeozoic giant dragonflies were hawker predators. Sci. Rep. *8*, 12141.

S3. Bechly, G., Brauckmann, C., Zessin, W., and Groning, E. (2001). New results concerning the morphology of the most ancient dragonflies (Insecta: Odonatoptera) from the Namurian of Hagen-Vorhalle (Germany). J. Zool. Syst. Evol. Res. *39*, 209–226.

S4. Gonzalez-Bellido, P.T., Peng, H., Yang, J., Georgopoulos, A.P., and Olberg, R.M. (2013). Eight pairs of descending visual neurons in the dragonfly give wing motor centers accurate population vector of prey direction. Proc. Natl. Acad. Sci. *110*, 696–701.

S5. Wardill, T.J., Knowles, K., Barlow, L., Tapia, G., Nordström, K., Olberg, R.M., and Gonzalez-Bellido, P.T. (2015). The Killer Fly Hunger Games: Target Size and Speed Predict Decision to Pursuit. Brain. Behav. Evol. *86*, 28–37.

S6. Wardill, T.J., Fabian, S.T., Pettigrew, A.C., Stavenga, D.G., Nordström, K., and Gonzalez-Bellido, P.T. (2017). A Novel Interception Strategy in a Miniature Robber Fly with Extreme Visual Acuity. Curr. Biol. *27*, 854–859.

S7. Gengs, C., Leung, H.-T., Skingsley, D.R., Iovchev, M.I., Yin, Z., Semenov, E.P., Burg, M.G., Hardie, R.C., and Pak, W.L. (2002). The target of Drosophila photoreceptor synaptic transmission is a histamine-gated chloride channel encoded by ort (hclA). J. Biol. Chem. *277*, 42113–20.

S8. Gonzalez-Bellido, P.T., and Wardill, T.J. (2012). Labeling and Confocal Imaging of Neurons in Thick Invertebrate Tissue Samples. Cold Spring Harb. Protoc. *2012*, pdb.prot069625-pdb.prot069625.

S9. Preibisch, S., Saalfeld, S., and Tomancak, P. (2009). Globally optimal stitching of tiled 3D microscopic image acquisitions. Bioinformatics *25*, 1463–5.

S10. Schindelin, J., Arganda-Carreras, I., Frise, E., Kaynig, V., Longair, M., Pietzsch, T., Preibisch, S., Rueden, C., Saalfeld, S., Schmid, B., *et al.* (2012). Fiji: an open-source platform for biological-image analysis. Nat. Methods *9*, 676–682.

S11. Peng, H., Bria, A., Zhou, Z., Iannello, G., and Long, F. (2014). Extensible visualization and analysis for multidimensional images using Vaa3D. Nat. Protoc. *9*, 193–208.

S12. Bria, A., Iannello, G., Onofri, L., and Peng, H. (2016). TeraFly: real-time three-dimensional visualization and annotation of terabytes of multidimensional volumetric images. Nat. Methods *13*, 192–194.

S13. Wang, Y., Li, Q., Liu, L., Zhou, Z., Ruan, Z., Kong, L., Li, Y., Wang, Y., Zhong, N., Chai, R., *et al.* (2019). TeraVR empowers precise reconstruction of complete 3-D neuronal morphology in the whole brain. Nat. Commun. *10*, 3474.

Video S1

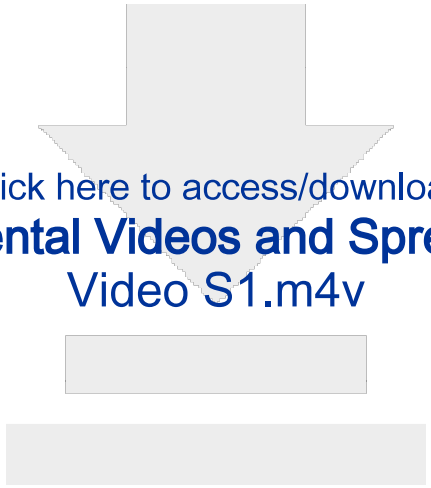

Click here to access/download

Supplemental Videos and Spreadsheets

Video S1.m4v

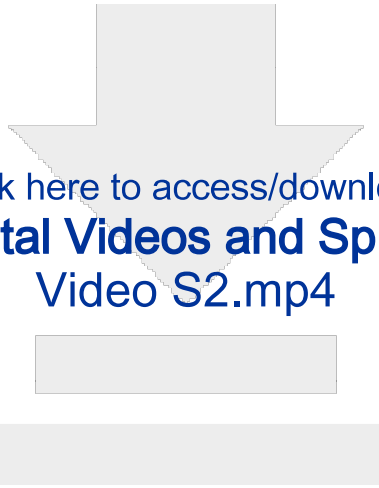

Click here to access/download

Supplemental Videos and Spreadsheets

Video S2.mp4

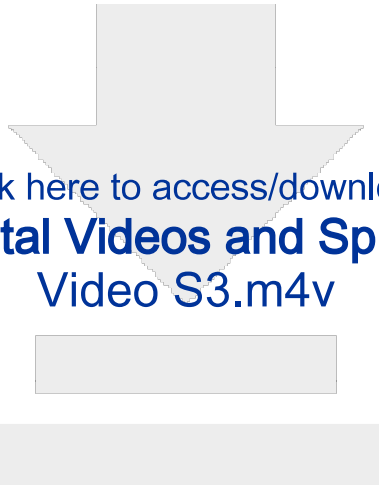

Click here to access/download

Supplemental Videos and Spreadsheets

Video S3.m4v

Click here to access/download

Supplemental Videos and Spreadsheets

Video S4.m4v